



Neutrino Properties with Ground-based Millimeter-wavelength Line Intensity Mapping

Azadeh Moradinezhad Dizgah¹ , Garrett K. Keating² , Kirit S. Karkare^{3,4} , Abigail Crites^{5,6}, and Shouvik Roy Choudhury⁷ ¹Département de Physique Théorique, Université de Genève, 24 quai Ernest Ansermet, 1211 Genève 4, Switzerland; azadeh.moradinezhaddizgah@unige.ch²Center for Astrophysics, Harvard & Smithsonian, 60 Garden Street, Cambridge, MA 02138, USA; garrett.keating@cfa.harvard.edu³Kavli Institute for Cosmological Physics, University of Chicago, 5640 S. Ellis Ave., Chicago, IL 60637, USA⁴Fermi National Accelerator Laboratory, MS209, P.O. Box 500, Batavia, IL 60510, USA⁵Department of Physics, Cornell University, 109 Clark Hall, Ithaca, NY 14853, USA⁶Department of Physics, California Institute of Technology, 1200 E. California Blvd., Pasadena, CA 91125, USA⁷Department of Physics, Indian Institute of Technology Bombay, Main Gate Road, Powai, Mumbai 400076, India

Received 2021 October 11; revised 2021 November 29; accepted 2021 November 29; published 2022 February 18

Abstract

Line intensity mapping (LIM) is emerging as a powerful technique to map the cosmic large-scale structure and to probe cosmology over a wide range of redshifts and spatial scales. We perform Fisher forecasts to determine the optimal design of wide-field ground-based millimeter-wavelength LIM surveys for constraining properties of neutrinos and light relics. We consider measuring the auto-power spectra of several CO rotational lines (from $J = 2-1$ to $J = 6-5$) and the [C II] fine-structure line in the redshift range of $0.25 < z < 12$. We study the constraints with and without interloper lines as a source of noise in our analysis, and for several one-parameter and multiparameter extensions of Λ CDM. We show that LIM surveys deployable this decade, in combination with existing cosmic microwave background (CMB; primary) data, could achieve order-of-magnitude improvements over Planck constraints on N_{eff} and M_{ν} . Compared to next-generation CMB and galaxy surveys, a LIM experiment of this scale could achieve bounds that are a factor of ~ 3 better than those forecasted for surveys such as EUCLID (galaxy clustering), and potentially exceed the constraining power of CMB-S4 by a factor of ~ 1.5 and ~ 3 for N_{eff} and M_{ν} , respectively. We show that the forecasted constraints are not substantially affected when enlarging the parameter space, and additionally demonstrate that such a survey could also be used to measure Λ CDM parameters and the dark energy equation of state exquisitely well.

Unified Astronomy Thesaurus concepts: Cosmology (343); Large-scale structure of the universe (902); Cosmological parameters (339); Cosmological neutrinos (338)

1. Introduction

Neutrinos are among the most abundant particles in the universe, and thus affect different epochs in the cosmic history. Cosmological observations are sensitive to the effective number of neutrinos, N_{eff} , when they were still relativistic and contributed to the radiation content of the universe, as well as their total mass, $M_{\nu} \equiv \sum m_{\nu}$, when they became nonrelativistic and contribute to the matter content (Abazajian et al. 2016; Lattanzi & Gerbino 2018; Lesgourgues et al. 2013). The standard model of particle physics predicts three species of massless neutrinos, corresponding to $N_{\text{eff}}^{\text{SM}} = 3.046$ (Mangano et al. 2005; Grohs et al. 2016; de Salas & Pastor 2016). While the current best constraint on N_{eff} from the cosmic microwave background (CMB; Ade et al. 2019) is consistent with this prediction, neutrino flavor oscillation experiments, which have measured nonzero neutrino mass splittings (de Salas et al. 2018; Esteban et al. 2019), provide striking evidence in favor of physics beyond the standard model (BSM) to describe the origin of nonzero neutrino masses.

Next-generation CMB experiments (Ade et al. 2019; Abazajian et al. 2016) are expected to provide stringent constraints on N_{eff} (Green et al. 2019). Observations of large-scale structure (LSS) will be complementary to CMB, particularly in ameliorating parameter degeneracies (e.g., between N_{eff} and Λ CDM parameters as well as with the sum of neutrino masses and

primordial Helium abundance; Baumann et al. 2018; Sprenger et al. 2019; DePorzio et al. 2021). Since N_{eff} measures the total energy density in radiation excluding photons, a high-significance detection of an excess light relic abundance, $N_{\text{eff}} = N_{\text{eff}}^{\text{SM}} + \Delta N_{\text{eff}}$, offers a discovery space for BSM physics: many extensions to the SM predict extra light relics, for example axions (Baumann et al. 2016) and light sterile neutrinos (Abazajian et al. 2012; Archidiacono et al. 2015). The contribution of light thermal relics to N_{eff} is determined by their number of spin states and decoupling temperatures. As such, there is a minimum contribution to N_{eff} from light relics that decoupled prior to the QCD phase transition, $\Delta N_{\text{eff}} \geq 0.027$ (Brust et al. 2013; Chacko et al. 2015), which sets a theoretical target sensitivity for upcoming surveys.

In contrast to N_{eff} , constraining the total mass of neutrinos from CMB primary anisotropies is challenging since neutrinos with sub-eV mass are still relativistic around the last-scattering surface, and thus their mass affects the CMB weakly. On the other hand, gravitational lensing of the CMB, which indirectly probes the underlying dark matter distribution, is a sensitive probe of neutrino masses. But several parameter degeneracies—most notably between M_{ν} , the total matter density and optical depth (Allison et al. 2015; Liu et al. 2016), and between M_{ν} and the dark energy (DE) equation of state (EoS; Hannestad 2005; Roy Choudhury & Hannestad 2020)—limit the potential of upcoming CMB surveys (Ade et al. 2019; Abazajian et al. 2016; Sugai et al. 2020) in constraining M_{ν} . Biased tracers of LSS provide the most promising window to probe massive neutrinos via their imprints on the expansion history and growth of structure using various statistics, including auto- and cross-



Original content from this work may be used under the terms of the [Creative Commons Attribution 4.0 licence](https://creativecommons.org/licenses/by/4.0/). Any further distribution of this work must maintain attribution to the author(s) and the title of the work, journal citation and DOI.

correlations between different probes (Boyle & Komatsu 2018; Schmittfull & Seljak 2018; Yu et al. 2018; Chudaykin & Ivanov 2019; Dvorkin et al. 2019; Hahn et al. 2020; Boyle & Schmidt 2021; Massara et al. 2021; Hahn & Villaescusa-Navarro 2021; Bayer et al. 2021b; Chen et al. 2021b). The measurements of mass splitting by neutrino flavor oscillation experiments,⁸ which set a minimum for the sum of neutrino masses, $M_\nu = 0.059$ eV in the normal and $M_\nu = 0.10$ eV in the inverted mass hierarchies, provide theoretical thresholds for future cosmological measurements of M_ν .

In addition to the shape and clustering of galaxies and CMB secondary anisotropies, line intensity mapping (LIM) is emerging as a viable probe of LSS (Kovetz et al. 2017). Measuring spatial fluctuations in the brightness temperature of spectral lines together with their observed frequencies provides a low-resolution, three-dimensional map of LSS. LIM experiments can efficiently survey large sky fractions and extended redshift ranges, largely inaccessible to traditional galaxy surveys. The promise of LIM in constraining cosmological parameters is threefold. First, the large comoving volume probed by LIM surveys significantly lowers statistical uncertainty on model parameters. Second, at the higher redshifts uniquely probed by LIM, we access a larger number of modes in the linear and quasi-linear regimes since gravitationally induced nonlinearities are smaller. Therefore, line clustering statistics can be accurately described by perturbation theory over a wider range of scales, allowing for robust and high-precision cosmological constraints. Third, the wide redshift coverage of LIM surveys allows for efficiently breaking parameter degeneracies present in the CMB and lower-redshift probes of LSS (Archidiacono et al. 2017; Lorenz et al. 2017; Obuljen et al. 2018; Sprenger et al. 2019).

Besides the 21 cm hyperfine transition of neutral hydrogen, the rotational lines of carbon monoxide, CO, (Righi et al. 2008; Lidz et al. 2011; Breyse et al. 2014; Li et al. 2016; Fonseca et al. 2017; Padmanabhan 2018), and the fine-structure line of ionized carbon, [C II], (Gong et al. 2011; Silva et al. 2015; Fonseca et al. 2017; Pullen et al. 2018; Padmanabhan 2019) are among the most-studied target lines in the context of galaxy and star formation. More recently, some of their potential in constraining cosmology has also been explored (Karkare & Bird 2018; Creque-Sarbinowski & Kamionkowski 2018; Moradinezhad Dizgah et al. 2019; Moradinezhad Dizgah & Keating 2019; Liu & Breyse 2021; Gong et al. 2020; Bernal et al. 2021, 2021). The first detections of 21 cm (Masui et al. 2013), CO (Keating et al. 2015, 2016, 2020) and [C II] (Pullen et al. 2018), have amplified this growing interest in LIM. Current planned surveys, such as COMAP (Li et al. 2016), CCAT-Prime (Herter et al. 2019), CONCERTO (Lagache et al. 2018), and TIME (Crities et al. 2014) are expected to provide first robust detections of the CO/[C II] clustering power spectra. These data, however, will have limited utility in constraining cosmology. Theoretical guidance for the design of wide-field LIM surveys, capable of reaching the required target sensitivities on various cosmological parameters, is therefore essential.

In this paper, we explore constraining neutrino properties using ground-based millimeter-wave LIM observations, in particular focusing on next-generation instrument configurations that could feasibly be deployed in the next decade. New detector technologies are now being demonstrated that could provide the order-of-magnitude sensitivity improvements over current-generation experiments at a reasonable cost. We therefore explore the constraining power over a wide range of experimental sensitivities that encompass the possible experiments that could be fielded. We forecast the expected uncertainties on M_ν and N_{eff} as a function of survey cost (parameterized as a product of spectrometer count and observing time) when only a 1-parameter extension of Λ CDM is considered, as well as when multiple degenerate, beyond- Λ CDM parameters are varied.

The rest of the paper is organized as follows. We review the physical effects of neutrino properties on LSS in Section 2. We then describe the model of the line intensity power spectrum in Section 3, and outline the instrument and survey specifications in Section 4. After describing the details of our analysis methodology in Section 5, we present our results in Section 6, and conclude in Section 7. Supplementary information is provided in two appendices. In Appendix A, we give details of redshift binning and instrument noise, and in Appendix B, we compare forecasted parameter constraints from LIM with those from EUCLID, showing 2D marginalized errors and reporting the constraints on all model parameters.

2. Imprints of Neutrinos on Large-scale Structure

Neutrinos affect cosmological observables through background and perturbation effects (Lesgourgues et al. 2013). In this section, we review various imprints of the effective number of neutrinos (light relics more generally) and their mass on LSS, highlighted in the existing literature. We also emphasize some unique advantages of LIM in shedding light on neutrino properties.

2.1. Effective Number of Light Relics

Keeping the redshift of matter-radiation equality and baryon density fixed, the primary background effects of increasing N_{eff} on LSS are an enhancement of the matter power spectrum on small scales and a damping of the baryon acoustic oscillation (BAO) amplitude, arising from the decrease of the ratio of baryons to cold dark matter (CDM). At the level of perturbations, higher N_{eff} shifts the BAO phase and lowers its amplitude. During the radiation-dominated era, the presence of free-streaming neutrinos significantly reduces the metric fluctuations (within the free-streaming scale), which drive oscillations in the photon-baryon fluid (Hu & Sugiyama 1996). Furthermore, the propagation of neutrino perturbations at the speed of light *drags* perturbations in the photon-baryon fluid, which propagate at the speed of sound, shifting the CMB acoustic peaks (Bashinsky & Seljak 2004). These effects are then imprinted on the baryon fluctuations prior to baryon drag time and later in the matter power spectrum through the BAO feature. The BAO phase shift, which has been measured in both the CMB and LSS (Follin et al. 2015; Baumann et al. 2019), is a robust signature of light relics, difficult to mimic by changing the initial conditions or matter content, and is largely unaffected by the nonlinear gravitational evolution in the late universe (Baumann et al. 2017). However, constraints on N_{eff} from the BAO phase shift alone are shown to

⁸ Neutrino oscillation experiments to date (de Salas et al. 2018; Esteban et al. 2019) have measured two squared-mass differences between the three neutrino species, allowing for two possible mass hierarchies: normal (two light and one heavy) versus inverted (two heavy and one light). While recent results show a weak preference for the normal ordering (Abe et al. 2018a, 2018c; Acero et al. 2019), future neutrino experiments such as DUNE (Abi et al. 2020) and Hyper-K (Abe et al. 2018b) promise an unambiguous determination of the two hierarchies (see Patterson 2015 for a review of the experimental prospects).

be weaker than those from the full power spectrum shape (Baumann et al. 2018). We therefore consider the full shape of the line power spectrum.

2.2. Sum of Neutrino Masses

Massive neutrinos impact LSS in several ways. At the background level, they change the expansion history, which alters cosmological distance scales measured by the BAO feature or Alcock-Paczynski (AP) test (Pan & Knox 2015). As shown in Boyle & Komatsu (2018), constraints on neutrino masses from distance probes are weaker than those from the growth of the structure (i.e., the perturbation effects). Furthermore, due to various parameter degeneracies (e.g., between M_ν and spatial curvature Ω_k), BAO and AP constraints are significantly degraded once the parameter space is enlarged. At the level of perturbations, massive neutrinos affect the matter power spectrum in two ways. On scales below their free-streaming scale, they do not contribute to the gravitational clustering due to their large thermal velocities. Meanwhile, their background density contributes to the homogeneous expansion, slowing down the growth of clustering of matter fluctuations (Bond et al. 1980; Hu & Eisenstein 1998). These two effects lead to the suppression of the matter power spectrum below the neutrino free-streaming scale (Hu et al. 1998). On scales larger than the free-streaming scale of neutrinos when they become nonrelativistic, the matter power spectrum is unaffected. Therefore, massive neutrinos render the growth rate of the structure—which can be measured by redshift-space distortions (RSD)—scale-dependent. In our forecasts, we include both the background and perturbation effects by considering the full shape of the line power spectrum in the redshift space, neglecting the nonlinear effects of the massive neutrinos (Brandbyge & Hannestad 2008; Bird et al. 2012; Castorina et al. 2015; Upadhye 2019; Hannestad et al. 2020; Garny et al. 2021; Garny & Taule 2021; Chen et al. 2021a; Bayer et al. 2021a).

When considering biased tracers (e.g., halos, galaxies, and line intensity), the scale-dependent growth rate of the structure in the presence of massive neutrinos induces a small scale-dependence of the linear bias of the tracer (LoVerde 2014),⁹ which can be accurately computed using tools provided by Muñoz & Dvorkin (2018) and Valcin et al. (2019). Apart from this physical scale-dependence of the linear bias, it was shown in Villaescusa-Navarro et al. (2014) and Castorina et al. (2014) that, in the presence of massive neutrinos, defining the halo bias with respect to the total matter overdensity, δ_m , results in a spurious scale-dependence of the linear bias, which can be removed if the bias is defined with respect to the CDM+baryon overdensity, δ_{cb} . Not accounting for this effect results in overestimating the total impact of the massive neutrinos on the power spectrum of biased tracers (Obuljen et al. 2018).¹⁰ Therefore, we define the line bias with respect to δ_{cb} , and neglect the physical scale-dependence of the linear bias. The latter simplification is justified since, on the scales where the effect is the most prominent, the contribution of nonlinear biasing of the line intensity fluctuations (which we have neglected) most likely dominates over this effect.

Lastly, in the presence of massive neutrinos, the change in the expansion history (resulting in a modification of the mean comoving density $\bar{\rho}$) and small-scale suppression of the matter power spectrum (resulting in a lower variance of matter fluctuations), also affect the halo abundance described by the halo mass function (HMF) by reducing the number of higher mass halos (Castorina et al. 2014; Biswas et al. 2019). By comparing cosmological simulations with and without massive neutrinos, it has been shown that in order to obtain a universal HMF, replacing δ_m with δ_{cb} is essential. An interesting fact relevant for LIM is that the impact of massive neutrinos on the mass function becomes more pronounced at higher redshifts. Since the line intensity fluctuations are a cumulative signal over contributions from all galaxies emitting a given line, in the halo model description, the line power spectrum is sensitive to the HMF. Therefore, this sensitivity offers LIM additional constraining power on neutrino masses. In particular, it is of interest to understand whether LIM across a wide z range can probe the redshift-dependent modification of the HMF due to massive neutrinos, and ameliorate the degeneracy between neutrino mass and variance of fluctuations σ_8 . We account for the above modification to the HMF in our forecast, but leave more detailed study of the significance of this redshift-dependence to future work.

2.3. Unique Advantages of LIM

We now highlight the unique capabilities of LIM in constraining N_{eff} and M_ν . Most obviously, LIM can provide significantly smaller statistical errors for both parameters than existing constraints by probing a larger comoving volume. For N_{eff} , combining LIM and CMB data significantly improves constraints by breaking degeneracies with Λ CDM parameters and the primordial Helium fraction, Y_{He} . The latter degeneracy is one of the main limiting factors for CMB observations, since both parameters alter the damping tail of the CMB power spectrum by changing the early time Hubble parameter. On the contrary, as for other tracers of LSS, line intensity fluctuations are largely insensitive to Y_{He} . For M_ν , the wide redshift coverage of LIM plays a more significant role than for N_{eff} . The reason is twofold: first, while the suppression of the small-scale matter power spectrum decreases at higher redshift, the suppression of the growth rate is more prominent at higher redshift.¹¹ Therefore, with a long redshift arm, LIM surveys provide a powerful means to maximally capture information from the two signatures. Second, measuring both high- and low-redshift information breaks parameter degeneracies present in the CMB and low-redshift observables. For instance, constraining the amplitude of fluctuations over a long redshift range with LIM (Schmittfull & Seljak 2018; Yu et al. 2018), and probing LSS at the redshifts where the impact of DE is less important, lead to an enhanced sensitivity to M_ν .

It should be kept in mind that, when considering LIM with a single emission line, the large uncertainties on the nuisance astrophysical parameters (i.e., the mean brightness temperature and the bias of the line) can limit the constraining power since they are degenerate with cosmological parameters. As previously shown in the context of 21 cm intensity mapping, these degeneracies can be significantly alleviated in

⁹ Scale-dependence of the halo bias as a result of scale-dependent growth was first studied in Hui & Parfrey (2008) and Parfrey et al. (2011) in the context of modified gravity.

¹⁰ For instance, for the combined EUCLID+HIRAX data, it was shown in Obuljen et al. (2018) that this effect can lead to degradation of the errors by roughly 30%.

¹¹ The latter is because, at higher redshifts, the effect of neutrino free-streaming has had less time to accumulate, while the former is because, once neutrinos become nonrelativistic at low redshifts, they cease to affect the growth rate.

two ways: first, by modeling the line signal at higher order in perturbation theory and extending the analysis to smaller scales (Castorina & White 2019); second, by taking advantage of cross-correlations between intensity maps and other cosmological probes, such as optical galaxy surveys and CMB lensing (Obuljen et al. 2018; Chen et al. 2019). For the multiline LIM survey we consider here, measuring cross-correlations between lines in the same survey, in addition to the auto-correlations of individual lines, provides an internal means to break the aforementioned degeneracies. In this paper, we use a linear model of the line power spectrum, assume that tight priors on the line biases and mean brightness temperatures are available, and set them to their theoretically predicted values. We leave for future work a quantitative study of the impact of these degeneracies on forecasted constraints, and the precision of the priors that the cross-correlations can provide.

3. The Power Spectrum of Line Intensity Fluctuations

CO is predominantly found in the dense clouds of molecular gas (of density $\sim 10^3 \text{ cm}^{-3}$), while [C II] emission can originate from a variety of environments (Goldsmith et al. 2012; Lagache et al. 2018). Both are typically tracers of the cool gas, within galaxies, that provides the fuel for star formation, and the strength of their emission is observed to be correlated with the star formation rates (SFRs) of galaxies (Tacconi et al. 2013b; Herrera-Camus et al. 2015).

We use a simple model for the line intensity signal, commonly used in the literature, in which the mean and fluctuations of the line intensity are related to the abundance of halos that host CO- or [C II]-luminous galaxies (Visbal & Loeb 2010; Gong et al. 2011; Lidz et al. 2011; Silva et al. 2015); see also Popping et al. (2016), Vallini et al. (2018), Popping et al. (2019), Lagache et al. (2018), Yang et al. (2021), and references therein for more detailed modeling of CO and [C II] based on semi-analytical models in combination with hydrodynamical simulations.

The mean brightness temperature (typically in units of μK) at redshift z is given by

$$\bar{T}_{\text{line}}(z) = \frac{c^2 p_{1,\sigma}}{2k_B \nu_{\text{obs}}^2} \int_{M_{\text{min}}}^{M_{\text{max}}} dM \frac{dn}{dM} \frac{L_{\text{line}}(M, z)}{4\pi \mathcal{D}_L^2} \left(\frac{dl}{d\theta} \right)^2 \frac{d\theta}{d\nu}, \quad (1)$$

where M_{min} and M_{max} are the minimum and maximum masses of the halos that host galaxies emitting in a given line, c is the speed of light, k_B is the Boltzmann factor, ν_{obs} is the observed frequency of the line, dn/dM is the HMF, L_{line} is the specific luminosity of the line-emitting galaxy located in a halo of mass M at redshift z , and \mathcal{D}_L is the luminosity distance. The terms $dl/d\theta$ and $d\theta/d\nu$ reflect the conversion from units of comoving lengths, l , to those of the observed specific intensity: frequency, ν , and angular size, θ . The term $dl/d\theta$ is equivalent to the comoving angular diameter distance and

$$\frac{dl}{d\nu} = \frac{c(1+z)}{\nu_{\text{obs}} H(z)}, \quad (2)$$

where $H(z)$ is the Hubble parameter at a given redshift. The parameter $p_{1,\sigma}$ accounts for scatter in the relations between SFR and the specific luminosity with halo mass (Li et al. 2016;

Keating et al. 2016) and is given by

$$p_{n,\sigma} = \int_{-\infty}^{\infty} dx \frac{10^{nx}}{\sqrt{2\pi} \sigma_{\text{line}}} e^{-x^2/2\sigma_{\text{line}}^2}, \quad (3)$$

with $n=1$ for the mean temperature and $n=2$ for the shot-noise contribution, as discussed below. We set the value of $\sigma_{\text{line}}=0.37$ for both CO and [C II], corresponding to the fiducial model of Li et al. (2016) and in reasonable agreement with observational studies (Speagle et al. 2014; Carilli & Walter 2013; Kamenetzky et al. 2016; Sargsyan et al. 2012).

We model the CO luminosity by assuming scaling relations between CO and far-infrared (FIR) luminosities and between the FIR luminosity and SFR, following Li et al. (2016). We use the empirical fit of Behroozi et al. (2013) to relate the SFR and the halo mass and redshift. At $z > 8$, we extrapolate the SFR fit at lower redshift according to

$$\log \text{SFR}(M, z) = \min[\text{SFR}(M, z=8) + 0.2943(z-8), 3.3847 - (0.2413z)]. \quad (4)$$

The SFR (in units of $M_{\odot} \text{ yr}^{-1}$) is related to the total infrared luminosity L_{IR} (in units of L_{\odot}) via the Kennicutt relation (Kennicutt 1998) of the form

$$\text{SFR}(M, z) = \delta_{\text{MF}} \times 10^{-10} L_{\text{IR}}, \quad (5)$$

where the normalization depends on the assumptions of the initial mass function, the duration of star formation, etc. As in Behroozi et al. (2013) and Li et al. (2016), we take $\delta_{\text{MF}}=1$. The FIR luminosity L_{IR} (in units of L_{\odot}) is then related to the CO line luminosity L'_{CO} (in units of $\text{K km s}^{-1} \text{ pc}^2$), through a power-law fit of the form

$$\log L_{\text{IR}} = \alpha \log L'_{\text{CO}} + \beta. \quad (6)$$

We use the results of Kamenetzky et al. (2016), which provide empirical fits for the above relation for the CO rotational ladder using Herschel SPIRE Fourier Transform Spectrometer data. The CO line luminosity can then be expressed (in units of L_{\odot}) via the following expression:

$$L_{\text{CO}(J \rightarrow J-1)} = 4.9 \times 10^{-5} J^3 L'_{\text{CO}(J \rightarrow J-1)}. \quad (7)$$

In modeling the luminosity of [C II]-luminous galaxies, we use the results of Silva et al. (2015), which relate the [C II] luminosity to the SFR via a power-law scaling relationship, where

$$\log L_{[\text{CII}]} = a_{L[\text{CII}]} \times \log \text{SFR}(M, z) + b_{L[\text{CII}]}. \quad (8)$$

We set the values of $a_{L[\text{CII}]}=0.8475$ and $b_{L[\text{CII}]}=7.2203$ (their model m_1), which correspond to the fit to high-redshift galaxies by De Looze et al. (2014). We adopt the same SFR as for the CO lines. In Figure 1, we show the mean brightness temperature as a function of redshift for [C II] and the first six rotational lines of CO (see also Figure 4 for the mean brightness temperature in frequency space).

The total observed power spectrum of fluctuations in a given line, i.e., the signal of interest (s), has three contributions: clustering, shot, and instrumental noise,

$$P_{\text{tot}}(k, \mu, z) = P_{\text{clust}}^s(k, \mu, z) + P_{\text{shot}}^s(z) + P_N. \quad (9)$$

Here μ is the cosine of the angle between a given wavenumber and the line-of-sight direction. The clustering contribution (typically in units of $\mu\text{K}^2 \text{ Mpc}^{-3} h^3$) is anisotropic

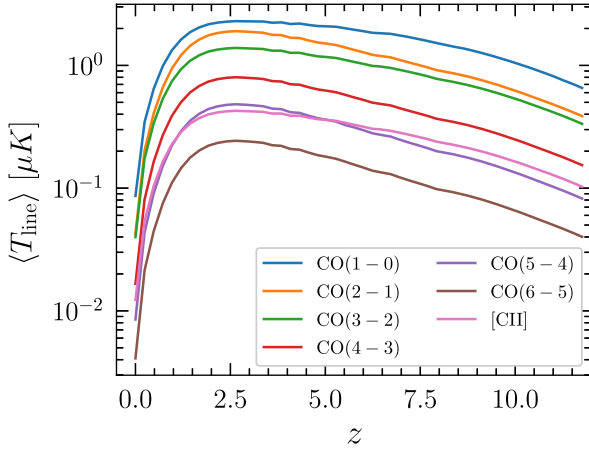


Figure 1. Mean brightness temperature as a function of redshift for spectral lines considered in this work.

due to RSD and the AP effect, and on large scales can be modeled as

$$P_{\text{clust}}^s(k, \mu, z) = \frac{H_{\text{true}}(z)}{H_{\text{ref}}(z)} \left[\frac{D_{A,\text{ref}}(z)}{D_{A,\text{true}}(z)} \right]^2 \times [1 + \mu_{\text{true}}^2 \beta(k_{\text{true}}, z)]^2 \exp\left(-\frac{k_{\text{true}}^2 \mu_{\text{true}}^2 \sigma_v^2}{H^2(z)}\right) \times [\bar{T}_{\text{line}}(z)]^2 b_{\text{line}}^2(z) P_0(k_{\text{true}}, z), \quad (10)$$

where $\beta = f/b_{\text{line}}$, and $f = d \ln D(k, z)/d \ln a$ is the growth rate of the structure with $D(k, z)$ the growth factor and a the scale factor. Converting the measured redshifts and angular positions to three-dimensional comoving coordinates requires making an assumption of a *reference* cosmology. The AP effect refers to the apparent anisotropy in the observed power spectrum induced by the discrepancy between the reference cosmology and the *true* cosmology, which distorts the radial and transverse distances differently. In Equation (10), this is modeled by an overall volume rescaling factor in the first line, and by evaluating the second and third lines at the wavenumber and angles in the true cosmology ($k_{\text{true}}, \mu_{\text{true}}$), which are related to those in the reference cosmology (k, μ) by

$$k_{\text{true}} = k \left[(1 - \mu^2) \frac{D_{A,\text{ref}}^2(z)}{D_{A,\text{true}}^2(z)} + \mu^2 \frac{H_{\text{true}}^2(z)}{H_{\text{ref}}^2(z)} \right]^{1/2}, \quad \mu_{\text{true}} = \frac{k\mu}{k_{\text{true}}} \frac{H_{\text{true}}(z)}{H_{\text{ref}}(z)}. \quad (11)$$

The factors in the second line of Equation (10) account for RSD, i.e., distortions induced by the peculiar velocities of galaxies emitting a given line. The first is the linear Kaiser term accounting for enhancement of power on large scales, while the second is the suppression of power on small scales, i.e., the Finger of God (FoG) effect. The effect of the intrinsic line width of individual emitters, over which the emission is smeared out (as discussed in Keating et al. (2020)), can be described similarly to the FoG suppression. Therefore, we have

$$\sigma_v^2 = (1 + z)^2 \left[\frac{\sigma_{\text{FoG}}^2(z)}{2} + c^2 \sigma_z^2 \right], \quad (12)$$

where

$$\sigma_{\text{FoG}}(z) = \sigma_{\text{FoG},0} \sqrt{1 + z}. \quad (13)$$

For both CO and [C II], we assume that the bulk of the emitters have line widths of 300 km s^{-1} , approximately matching those for typically observed CO-bright galaxies at high redshift (Tacconi et al. 2013a), and corresponding to a value of $\sigma_z = 0.001(1 + z)$. We vary $\sigma_{\text{FoG},0}$ as a free parameter in our forecasts.

Finally, the third line of Equation (10) is the real-space clustering power spectrum with $P_0(k, z)$ the linear dark matter power spectrum, and $b_{\text{line}}(z)$ the luminosity-weighted bias of the line intensity, related to the bias of halos with mass M at redshift z , $b_h(M, z)$ as

$$b_{\text{line}}(z) = \frac{\int_{M_{\text{min}}}^{M_{\text{max}}} dM \frac{dn}{dM} b_h(M, z) L_{\text{line}}(M, z)}{\int_{M_{\text{min}}}^{M_{\text{max}}} dM \frac{dn}{dM} L_{\text{line}}(M, z)}. \quad (14)$$

In the Poisson limit, the shot-noise contribution to the line power spectrum arising from the discrete nature of the sources of line emission is given by

$$P_{\text{shot}}^s(z) = \frac{c^4 p_{2,\sigma}}{4k_B^2 \nu_{\text{obs}}^4} \int_{M_{\text{min}}}^{M_{\text{max}}} dM \frac{dn}{dM} \times \left[\frac{L_{\text{line}}(M, z)}{4\pi D_L^2} \left(\frac{dl}{d\theta} \right)^2 \frac{dl}{dv} \right]^2, \quad (15)$$

where $p_{2,\sigma}$ is given by Equation (3) for $n = 2$.

To illustrate the relative amplitudes of the lines considered in our forecasts, in Figure 2, we plot the clustering (solid lines) and shot components (dotted lines) of the CO/[C II] power spectra at $z = 2$ (left) and $z = 8$ (right). For the clustering contribution, we show the monopole, averaged over the angle μ . Note the change in relative amplitude of [C II] and CO(5-4) between the two redshifts. This is in agreement with the crossover seen at $z \sim 5$ in Figure 1, with [C II] becoming brighter than CO(5-4) at higher redshift. To better illustrate the redshift evolution of [C II], we show the angle-averaged [C II] power spectrum in Figure 3. The amplitude first increases and then decreases with increasing redshift. This behavior is largely driven by star formation history, although the redshift evolution of the line bias, matter fluctuations, and growth rate also have an impact.

Before closing this section, we note two aspects of the line power spectrum model used in this paper that will be improved in future, more realistic forecasts. First, for the clustering component in Equation (10), it is assumed that the matter fluctuations, the biasing relation of the line intensity, and the RSD can be described linearly. The linear model is clearly only valid on very large scales, and will be extended to include one-loop contributions. Second, the shot noise is assumed to be described by the Poisson approximation. Since on large scales the halo exclusion and small-scale nonlinearities are expected to produce sub-/super-Poissonian shot noise, the model will treat this correction as a nuisance parameter to be marginalized over. In the context of CO/[C II] LIM, these two aspects have been recently studied by Moradinezhad Dizgah et al. (2021), where the model predictions were tested against simulated intensity maps. Including these ingredients in the Fisher forecasts is likely to weaken the reported constraints on cosmological parameters, as has been shown in the context of intensity mapping of neutral hydrogen (Sailer et al. 2021).

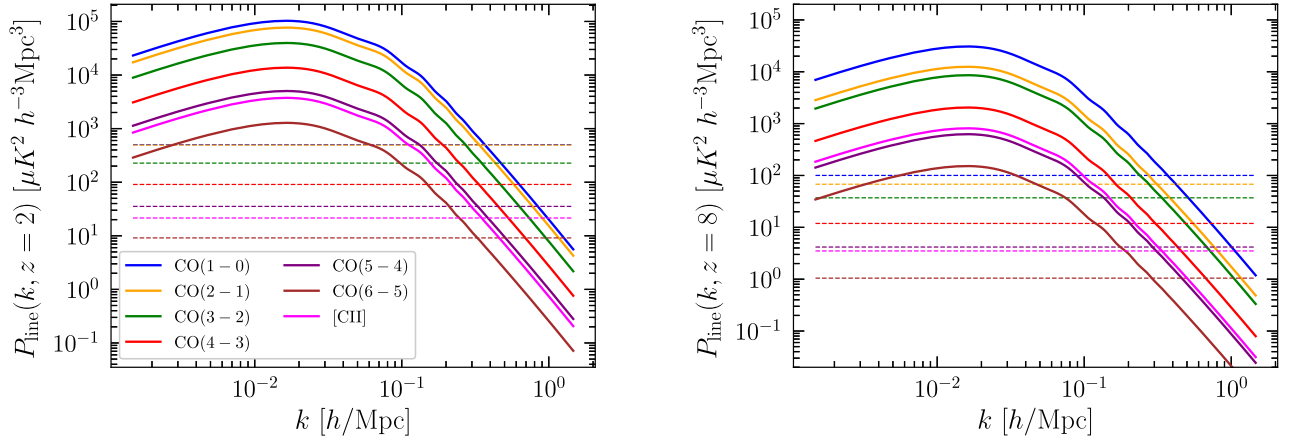


Figure 2. Angle-averaged clustering (solid lines) and shot-noise (dotted lines) contributions to the CO/[C II] line power spectra, at $z=2$ (left) and $z=8$ (right), for ΛCDM cosmology.

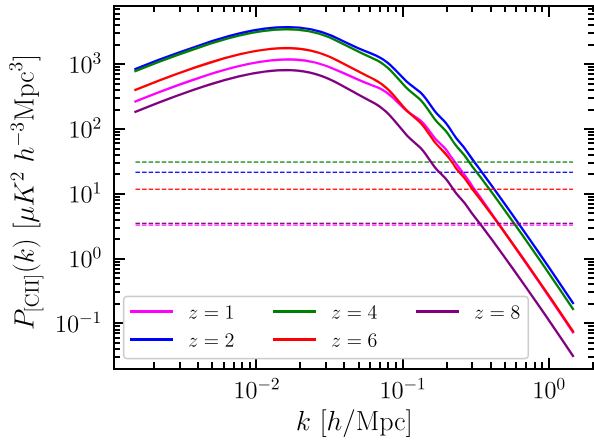


Figure 3. Redshift evolution of the angle-averaged [C II] power spectrum for ΛCDM cosmology.

4. Instrument Specifications, Survey Design, and Noise

In this section, we discuss the specifications of a hypothetical next-generation millimeter-wave LIM survey, and how those specifications translate into sensitivity estimates used in our forecasts.

In a LIM experiment, an image cube is generated by measuring the specific intensity at several sky positions, (l, m) , and frequencies, ν . A Fourier transform produces a 3D power spectrum, which can be further averaged down to a 1D spectrum like those seen in Figures 2 and 3 under the assumption of the cosmological principle. The noise on the individual modes of the power spectrum, P_N , can be related to the per-voxel noise, σ_N , of the original image cube:

$$P_N = \sigma_N^2 V_{\text{vox}}. \quad (16)$$

V_{vox} is the volume of individual voxels within the image cube, which can be further expressed as

$$V_{\text{vox}} = \Omega_{\text{vox}} \delta\nu \left(\frac{dl}{d\theta} \right)^2 \frac{dl}{d\nu}. \quad (17)$$

Here Ω_{vox} and $\delta\nu$ are the solid angle and bandwidth covered by a single voxel, respectively.

The sensitivity of our hypothetical survey is parameterized by *spectrometer-hours*, τ_{sh} , as a proxy for the *effort level* of an

experiment. If the survey area is Ω_s , such that the number of independent pointings is given by $\Omega_s/\Omega_{\text{vox}}$, then we can express Equation (16) as

$$P_N = \frac{\Omega_s \sigma_{\text{NET}}^2 \delta\nu}{\eta_{\text{opt}}^2 \tau_{\text{sh}}} \left(\frac{dl}{d\theta} \right)^2 \frac{dl}{d\nu}, \quad (18)$$

where σ_{NET} is the noise-equivalent temperature (NET) of the detector (units of $\text{K} \cdot \sqrt{\text{s}}$), and η_{opt} is the optical efficiency of the instrument.

For our analysis, we consider ground-based observations from an accessible observing site with excellent proven millimeter-wave observing conditions, such as the South Pole or the Atacama Desert. Figure 4 shows the atmospheric transmission as a function of frequency for median South Pole winter conditions, calculated using the *am* software (Paine 2019). In our projections, each individual spectrometer is sensitive to the full frequency range¹² between 80 and 310 GHz, encompassing the typical ground-based CMB atmospheric windows at 1, 2, and 3 mm; similar wide-bandwidth observations in a single receiver have been made with, e.g., SPT-3G (Anderson et al. 2019). We assume each spectrometer has a spectral resolution of $R = \nu/\Delta\nu = 300$, equivalent to what is now being demonstrated in the wideband millimeter-wave spectrometers (Redford et al. 2018; Karkare et al. 2020). The instrument is assumed to have a 10 m aperture, similar to the South Pole Telescope. We assume an overall optical efficiency of 25%, typical of current CMB experiments, and that each spectrometer detects both polarizations.

In the last two decades, millimeter-wave detectors have been demonstrated with device noise contributions that are well below atmospheric noise at these sites, even for narrow spectroscopic channels. We therefore make the assumption that each spectrometer's noise is dominated by atmospheric emission, with a secondary contribution from the emissivity of the telescope reflector surface. We define Q_{tot} to be the power received by a single channel of the detector:

$$Q_{\text{tot}} = Q_{\text{sky}} + Q_{\text{tel}}, \quad (19)$$

¹² By “full frequency range”, we mean that each spectrometer is capable of measuring all individual spectral channels simultaneously. This is in contrast to, e.g., Fabry–Perot interferometers or Fourier transform spectrometers, which require multiple measurements at different delays to synthesize individual frequency channels, and thus have lower instantaneous throughput than the spectrometer considered here.

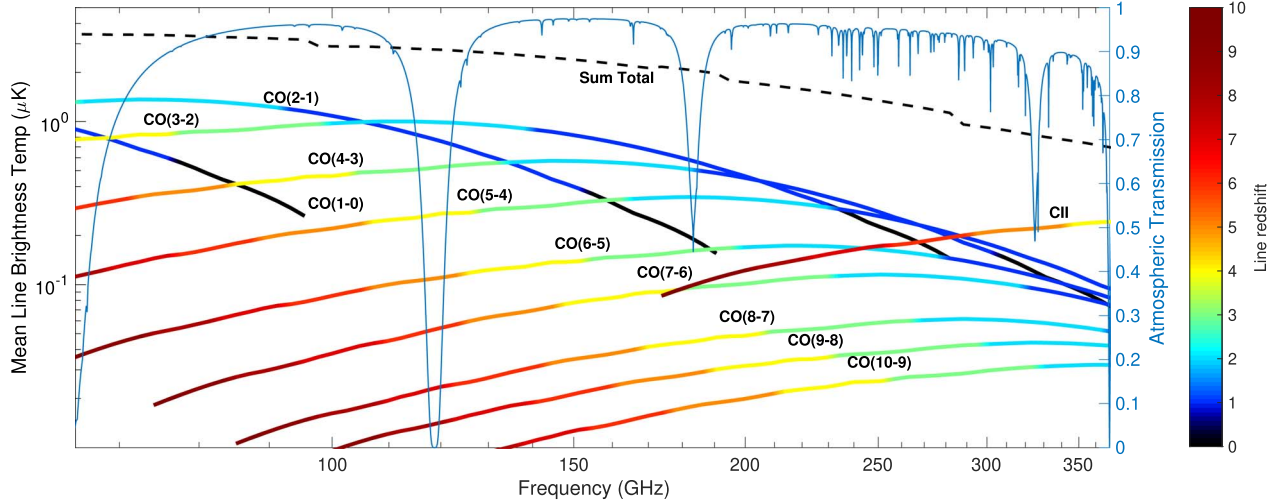


Figure 4. Spectral lines detectable by a ground-based survey. Shown above are model predictions for the brightness temperature of individual lines, their sum total (in dashed black), and atmospheric transmission (in light thin blue). The colors correspond to observed redshifts of the lines. The shown signal strengths adopt line luminosities scaled from the IR luminosity based on observational relations. Current constraints on these line ratios are uncertain by up to one order of magnitude.

where Q_{sky} and Q_{tel} are the noise power seen from the sky and the telescope, respectively. These individual contributions, under the assumption of single-mode, diffraction-limited optics, can be further expressed as

$$Q = \eta_{\text{opt}} \lambda_{\text{obs}}^2 \epsilon(\nu) \Delta \nu B(\nu, T). \quad (20)$$

Here, λ_{obs} is the observed wavelength, ϵ is the emissivity, and B is the Planck function, which varies as a function of frequency, ν , and temperature, T . We take the temperature to be 250 K for both the telescope and the atmosphere. The emissivity of the telescope is fixed at $\epsilon_{\text{tel}} = 0.01$, while the emissivity of the atmosphere ϵ_{atm} is calculated as a function of frequency, varying between 0.05 – 1 over the 80–310 GHz range. We can express the NET as

$$\sigma_{\text{NET}} = \frac{\sqrt{2Q_{\text{tot}} h \nu + (Q_{\text{tot}}^2 / \Delta \nu)}}{2k_B \eta_{\text{opt}} \Delta \nu (1 - \epsilon_{\text{tel}})(1 - \epsilon_{\text{atm}})}, \quad (21)$$

where h is the Planck constant. Typical NET values for our hypothetical instrument are of an order $\sim 1 \text{ mK} \cdot \sqrt{s}$ over the frequency range of interest. The NET can change substantially over the redshift window of a given line, particularly around the 118 GHz oxygen line or the 183 GHz water line. An optimal accounting for such variations in instrument noise are likely to be survey- and instrument-dependent, and is therefore beyond the scope of the work here. As a first-order approximation, we therefore take the median NET over a redshift window when evaluating Equation (16) for our Fisher analysis, and exclude frequency channels with NETs more than a factor of $\sqrt{2}$ greater than this median. The fraction of excluded channels is factored into the effective volume for each line and redshift combination (the use of which is discussed in Section 5).

As the optimal survey size varies as a function of survey sensitivity, for a given value of spectrometer-hours, we find the sky fraction that provides the tightest parameter constraints. This is evaluated over $17\text{--}17,000 \text{ deg}^2$. The minimum roughly corresponds to the smallest area that can be efficiently surveyed with a wide-field-of-view millimeter-wave camera, while the

maximum has recently been demonstrated by the Atacama Cosmology Telescope (ACT) from the Atacama Desert (Naess et al. 2020).

In our forecasts, we vary the spectrometer-hours over a wide range, starting with first-detection experiments and extending to larger-scale surveys that could be fielded in the next ten years. Current-generation instruments feature ~ 50 spectrometers (Crites et al. 2014) and are capable of completing surveys of order 10^5 spectrometer-hours. We therefore use this as a lower bound of the range considered here.

Current wide-bandwidth spectrometers either use a free-space diffraction grating that limits the number of detectors that can be placed in a cold volume or use a Fourier Transform spectrometer or Fabry–Perot interferometer, which do not simultaneously detect all frequencies independently. However, on-chip spectrometer technology—in which all frequencies are simultaneously and individually measured—can substantially improve the sensitivity. Current examples include SuperSpec/DESHIMA (filter-bank; Shirokoff et al. 2012; Endo et al. 2019) and μ -Spec (grating; Cataldo et al. 2012), all of which perform background-limited, wide-bandwidth spectroscopy on a few cm^2 of silicon. This technology will soon lead to filled spectroscopic focal planes similar in format to those used by CMB experiments. In several years, ~ 400 spectrometers could potentially be fielded in a single optics tube for planned multi-tube receivers. Future instruments could host anywhere from 7 (CCAT-prime; Herter et al. 2019) to 85 optics tubes (CMB-S4 LAT; Abazajian et al. 2019). CMB facilities at the South Pole and in Chile routinely accumulate several thousands of hours of integration time per year, and survey operations can extend for five years or more. We therefore forecast constraints for a wide range of spectrometer-hours, extending up to 4×10^9 .

As in Moradinezhad Dizgah & Keating (2019), we define an effective instrumental noise,

$$\tilde{P}_N(k, \mu, z) = \alpha_{\text{max}}^{-1}(k, \mu) \alpha_{\text{min}}^{-1}(k, \mu) P_N, \quad (22)$$

to account for attenuation of the signal due to the finite resolution of the instrument (α_{max}) and the finite redshift and angular coverage of the survey (α_{min}). The two attenuation factors are defined in terms of the largest and smallest recoverable modes in parallel and perpendicular to line-of-

sight directions,

$$\alpha_{\min}(k, \mu) = \alpha_{\min}(k_{\perp}, k_{\parallel}) \\ = (1 - e^{-k_{\perp}^2/(k_{\perp,\min}/2)^2})(1 - e^{-k_{\parallel}^2/(k_{\parallel,\min}/2)^2}), \quad (23)$$

$$\alpha_{\max}(k, \mu) = \alpha_{\max}(k_{\perp}, k_{\parallel}) = e^{-(k_{\perp}^2/k_{\perp,\max}^2 + k_{\parallel}^2/k_{\parallel,\max}^2)}, \quad (24)$$

where

$$k_{\parallel} = k\mu \quad k_{\perp} = k\sqrt{1 - \mu^2}. \quad (25)$$

The smallest recoverable modes are given by

$$k_{\max,\parallel} \approx 2\pi \left[\delta\nu \frac{dl}{d\nu} \right]^{-1}, \quad (26)$$

$$k_{\max,\perp} \approx 2\pi \left[\frac{c/\nu_{\text{obs}}}{D_{\text{ant}}} \frac{dl}{d\theta} \right]^{-1}, \quad (27)$$

where D_{ant} is the diameter of the aperture, and $\delta\nu$ is the spectral resolution of the instrument. The largest recoverable modes are given by

$$k_{\parallel,\min} = 2\pi\eta_{\min} \left[\nu_{\text{obs}} \frac{dl}{d\nu} \right]^{-1}, \quad (28)$$

$$k_{\perp,\min} \approx 2\pi \left[2 \sin(\theta_{\max}/2) \frac{dl}{d\theta} \right]^{-1}, \quad (29)$$

where $\theta_{\max} = \sqrt{\Omega_{\text{survey}}}$ is determined by the angular coverage of the survey, and η_{\min} is set by the redshift coverage of the survey. We set $D_{\text{ant}} = 10$ m, $\nu_{\text{obs}}/\delta\nu = 300$, and $\eta_{\min} = 3$, the latter of which is set by the frequency distance between high-opacity telluric lines (typically arising from oxygen and water, occurring at approximately 60, 118, 183, and 325 GHz in the millimeter-wave atmospheric window). Although in principle it may be possible to probe modes beyond this limit, this would require more sophisticated accounting for the effect of atmospheric windowing, and we conservatively assume that such modes are not practically accessible.

We note that our choice of D_{ant} and $\delta\nu$ are based on existing instrument parameters, although since we impose a conservative cutoff on the smallest-scale modes included in our forecasts ($k \gtrsim 0.3 h \text{ Mpc}^{-1}$; see Section 5), our results are expected to be relatively insensitive to these choices.

5. Analysis Methodology

We use the Fisher matrix formalism to perform parameter forecasts. For a given emission line, we split the survey into redshift bins with mean redshifts z_i and widths of 0.1 dex to account for the cosmic evolution of the line-emitting population, as well as variations in the instrument noise caused by the frequency-dependent atmospheric transmission (as discussed in Section 4). Neglecting correlations between redshift bins, for each emission line x , the total Fisher matrix is the sum of Fisher matrices of the individual redshift bins,

$$F_{\alpha\beta}^x = \sum_i F_{\alpha\beta}^{x,i} \quad (30)$$

with the Fisher matrix in the i th redshift bin given by

$$F_{\alpha\beta}^{x,i} = V_i \int_{-1}^1 \int_{k_{\min}}^{k_{\max}} \frac{k^2 dk d\mu}{8\pi^2} \text{Var}^{-1}[P_{\text{obs}}^x(k, \mu, z)] \\ \times \frac{\partial P_{\text{clust}}^x(k, \mu, z_i)}{\partial \lambda_{\alpha}} \frac{\partial P_{\text{clust}}^x(k, \mu, z_i)}{\partial \lambda_{\beta}}, \quad (31)$$

where λ are the model parameters that are varied. V_i is the volume of i th redshift bin extended between z_{\min} and z_{\max} and is proportional to sky coverage of the survey, f_{sky} , while $\text{Var}^{-1}[P_{\text{line}}^x]$ is the variance of the line power spectrum. The median redshifts of each bin and the corresponding instrument noise are given in Table 3 of Appendix A. The total Fisher matrix for all lines considered (i.e., CO from J=2-1 to J=6-5 and [C II]) is given by the sum of the Fisher matrices of individual lines, neglecting their cross-correlations, $F_{\alpha\beta}^{\text{tot}} = \sum_x F_{\alpha\beta}^x$.

We set the fiducial Λ CDM parameter values to those from the Planck 2018 data¹³ (Aghanim et al. 2020): $\ln(10^{10}A_s) = 3.0447$, $n_s = 0.96589$, $h = 0.6732$, $\Omega_{\text{cdm}} = 0.2654$, $\Omega_b = 0.04945$. For extension parameters, we set $N_{\text{eff}} = 3.046$, $M_{\nu} = 0.06$, $Y_{\text{He}} = 0.245398$, $w_0 = -1$, $w_a = 0$. For all forecasts, we assume three degenerate massive neutrino species.¹⁴ This choice is motivated by the recent results showing that the assumption of degenerate neutrinos is sufficiently accurate for current cosmological observations (Roy Choudhury & Hannestad 2020). It is also worth noting that, while high-precision measurement of M_{ν} by future surveys can rule out the inverted hierarchy, even future cosmological data alone will most likely not be able to directly detect the neutrino mass hierarchy (Archidiacono et al. 2020).¹⁵

We choose the fiducial value of $\sigma_{\text{FOG},0} = 250 \text{ km s}^{-1}$, and fix the line bias and mean brightness temperature to their theoretical values, accounting for their cosmology-dependence. We show results from LIM alone and in combination with Planck. For the latter, for each cosmology, we use the corresponding publicly available Planck 2018 MCMC chains¹⁶ to compute the parameter covariances and the Fisher matrix, marginalizing over optical depth. We assume the CMB and LIM Fisher matrices to be independent and add them to obtain the joint constraints. We use the CLASS code (Blas et al. 2011)¹⁷ to compute the matter power spectrum.

We compute k_{\min} from the largest recoverable modes in the parallel and perpendicular to line-of-sight directions given in Equations (26), (27):

$$k_{\min} = \sqrt{k_{\parallel,\min}^2 + k_{\perp,\min}^2}. \quad (32)$$

We set $k_{\max} = 0.15 \text{ Mpc}^{-1} h$ at $z = 0$. At higher redshifts, we obtain k_{\max} by finding the value that satisfies the following

¹³ Specifically, we use `base_plikHM_TTEEE_lowl_lowE`.

¹⁴ As first pointed out in Lesgourgues et al. (2004), considering three nondegenerate neutrinos and setting the mass of one (assuming an inverted hierarchy) or two (assuming a normal hierarchy) of them to zero, leads to observables significantly different from the true ones.

¹⁵ The weak evidence for the normal hierarchy in current data is almost entirely driven by the prior volume; the inverted hierarchy significantly reduces the size of parameter space (Hall & Challinor 2012).

¹⁶ <http://pla.esac.esa.int/pla/#cosmology>

¹⁷ <http://class-code.net>

condition for the variance of the linear matter density field:

$$\sigma^2(z) = \int_{k_{\min}(z)}^{k_{\max}(z)} \frac{d^3k}{(2\pi)^3} P_0(k, z) = \sigma^2(z=0). \quad (33)$$

This choice ensures that, at a given redshift, we are in the regime where fluctuations in the matter density are in the nearly linear regime where the perturbation theory is valid. We further impose a conservative upper bound of $k_{\max} \leq 0.3 \text{ Mpc}^{-1}h$ to ensure that our assumptions of linear bias and linear RSD (linear Kaiser term) are valid. Fisher matrices are evaluated for a given set of choices for f_{sky} and spectrometer-hours, combining constraints across all line species and redshift windows.

5.1. Impact of Interloper Lines

In a LIM survey, the voxel volume is defined in terms of the angular and frequency resolutions of the instrument, Equation (17). At a given redshift, in addition to the line of interest (i.e., the signal), the lines emitted from other redshifts projected onto the same observed frequency can be confused with the target signal in a given voxel. These contributions are referred to as interloper lines and can be accounted for as an additional source of noise in the measurement of the LIM power spectrum (Cheng et al. 2016; Gong et al. 2020). Accounting for interloper lines is particularly important for measuring the power spectrum at higher redshifts, as the interlopers at longer wavelengths (lower redshifts) can significantly contaminate the signal of interest. The difference in the redshifts of the signal and interlopers affects perpendicular and parallel line-of-sight distances differently. Therefore, the power spectra of interlopers observed at the signal's frequency are anisotropic even in the absence of RSD and the AP effect. Furthermore, in computing the power spectra of the projected interlopers, we must convert the comoving volume of the interlopers at their emission redshifts to the redshift of the signal at which they are observed.

Putting all this together, accounting for N interloper lines, the variance of the line signal power spectrum is given by

$$\begin{aligned} \text{Var}[P_{\text{obs}}(k, \mu, z)] &= \{P_{\text{clust}}^s(k, \mu, z) + P_{\text{shot}}^s(z) + \tilde{P}_N(k, \mu, z) \\ &+ \sum_i^N [A_{\perp}^i]^2 A_{\parallel}^i [P_{\text{clust}}^i(k_{\parallel}^i, k_{\perp}^i, z_i) + P_{\text{shot}}^i(z_i)]\}^2. \end{aligned} \quad (34)$$

The first three terms on the right-hand side of Equation (34) are the clustering and shot components of the line signal and instrumental noise, while the terms in the last line are the contributions from interloper lines. The factor of $[A_{\perp}^i]^2 A_{\parallel}^i$ accounts for the difference in the comoving volume due to interloper lines emitted from z_i with the volume of the line of interest at redshift z , given by

$$A_{\perp}^i = \frac{D_A(z)}{D_A(z_i)}, \quad A_{\parallel}^i = \frac{H(z_i)(1+z)}{H(z)(1+z_i)}. \quad (35)$$

The parallel and perpendicular components of the interloper wavevectors at their corresponding redshifts z_i are related to those of the source at redshift z by

$$\begin{aligned} k_{\parallel}^i(k, \mu) &= k \mu A_{\parallel}^i \\ k_{\perp}^i(k, \mu) &= k \sqrt{1 - \mu^2} A_{\perp}^i. \end{aligned} \quad (36)$$

Table 1
Models Considered in the Fisher Forecasts

Model	Parameters
1	$\Lambda\text{CDM} + N_{\text{eff}}$
2	$\Lambda\text{CDM} + M_{\nu}$
3	$\Lambda\text{CDM} + N_{\text{eff}} + M_{\nu}$
4	$\Lambda\text{CDM} + N_{\text{eff}} + Y_{\text{He}}$
5	$\text{CDM} + M_{\nu} + w_0$
6	$\text{CDM} + M_{\nu} + w_0 + w_a$

When neglecting the impact of interloper lines, the last line in Equation (34) is set to zero, and the variance is given by the sum of the clustering and shot contributions of the line of interest, and the instrumental noise.

Several techniques for reducing the impact of line interlopers have been proposed in the literature. This includes voxel masking (Breyse et al. 2015; Silva et al. 2015; Sun et al. 2018), cross-correlation (Lidz & Taylor 2016), spectral line deconfusion (Lidz & Taylor 2016; Cheng et al. 2016; Gong et al. 2020), and machine-learning (Moriwaki et al. 2020) or map-based deconfusion (Kogut et al. 2015; Cheng et al. 2020). With realistic component separation techniques, the contribution of interlopers to the variance of the power spectrum may be less than that implied by Equation (34), particularly with access to multiple lines in the same redshift window, as we do in the hypothetical instrument setup specified in Section 4. Due to a lack of observational data, the efficacy of such methods in the presence of the instrumentally and atmospherically induced spectral windowing functions is not yet known. Therefore, in our analysis, we consider two scenarios, which we expect will bracket the range of expectations with future analysis techniques. In the first, we consider Equation (34) as written (i.e., with interlopers present), and in the second, we neglect the P^i terms, effectively evaluating the power spectra as though no-interloper line species existed.

5.2. Parameter Degeneracies

Constraints on N_{eff} and M_{ν} can considerably degrade when enlarging the model parameter space (Archidiacono et al. 2017; Boyle & Komatsu 2018; Boyle & Schmidt 2021). Apart from degeneracies between N_{eff} , M_{ν} , and ΛCDM parameters, two other well-known degeneracies are between N_{eff} and Y_{He} in CMB data, and between M_{ν} and DE properties for both CMB and LSS probes at $z < 2$. To illustrate the strength of LIM in alleviating parameter degeneracies, we include six extensions to ΛCDM in our forecasts, described in Table 1.

We consider two models of DE beyond the cosmological constant: one with a constant EoS, and the other a dynamical DE model assuming the Chevallier–Linder–Polarski parameterization (Chevallier & Polarski 2001; Linder 2003), in which the redshift evolution of the DE EoS is given by

$$w(z) = w_0 + w_a \frac{z}{1+z}; \quad (37)$$

w_0 denotes the present-day value of the DE EoS. Thus, we vary w_0 in the first case, and w_0 and w_a in the second case. Varying the DE EoS parameter(s) along with M_{ν} is shown to degrade the bounds on M_{ν} from a “vanilla” $\Lambda\text{CDM} + M_{\nu}$ model (Hannestad 2005; Upadhye 2019; Lorenz et al. 2017; Mishra-Sharma et al. 2018; Brinckmann et al. 2019; Roy Choudhury & Hannestad 2020). However, an exception to this

rule occurs when the phantom part of the DE EoS parameter space ($w(z) \leq -1$) is excluded from the analysis: due to the parameter degeneracies, the nonphantom part of the parameter space prefers lower neutrino masses than $\Lambda\text{CDM} + M_\nu$ (see, e.g., Vagnozzi et al. 2018; Roy Choudhury & Naskar 2019). We do not consider a nonphantom-only model in this work.

The significant degeneracy between M_ν and the DE properties in CMB data originates from a geometric degeneracy: given that the CMB tightly constrains the comoving distance to the last-scattering surface, and that the present-day CMB photon density and the total CDM+baryon density are tightly constrained by the COBE/FIRAS temperature and CMB acoustic peaks, respectively, any change in comoving distance to the last-scattering surface due to the change in the DE EoS parameter(s) must be compensated by changes to the Hubble parameter and M_ν . For LSS observables at low redshifts ($z < 2$) when DE provides an important contribution to the energy density of the universe, M_ν and the DE EoS parameter(s) are correlated since they both modify the expansion rate and the growth of structure. Measurement of LSS observables at multiple redshifts is critical to alleviating this degeneracy (see, e.g., Mishra-Sharma et al. 2018).

5.3. Optimization Strategy

For each combination of interloper scenario and choice of cosmology, we calculate constraints on the parameter of interest (either N_{eff} or M_ν) while varying f_{sky} and spectrometer-hours, both with and without the addition of the Planck priors. We vary f_{sky} between 0.004 and 0.4096, stepping by factors of two, and spectrometer-hours between 2×10^5 and 4×10^9 , stepping by factors of three, and calculate constraints for a total of 110 observational setups for each of the 24 scenarios considered in our analysis. These constraints are then interpolated using a bicubic interpolation scheme, to estimate the optimal choice of f_{sky} (and expected value of $\sigma(N_{\text{eff}})$ or $\sigma(M_\nu)$), given a number of spectrometer-hours.

6. Results

In this section, we present the results of our forecasts, discussing the constraints on N_{eff} and M_ν separately.

6.1. Effective Number of Light Relics

In the top row of Figure 5, as a function of spectrometer-hours, we show the best-achievable 1σ constraint on N_{eff} (in blue) and the optimal sky area for that constraint (in red). In the two bottom rows, we show the constant 1σ contours in the plane of survey area versus spectrometer-hours, accounting for interlopers (middle), and neglecting them (bottom). The columns show the constraints when varying only N_{eff} (left), varying it simultaneously with M_ν (middle), or with Y_{He} (right). In the top rows, the gray horizontal lines are Planck-only constraints, with the lighter lines corresponding to LIM-only constraints, while darker lines are obtained from the combination of Planck and LIM. The dotted lines show the constraints with the effects of interloper emission included, while the dashed lines show the constraints with these effects neglected. The main observations can be summarized as follows:

1. Considering LIM alone and neglecting the interlopers (light dashed lines in the top row), for all three cosmologies, $\sigma(N_{\text{eff}})$ decreases as a power law when increasing the number of spectrometer-hours, τ_{sh} . Simultaneous variation

of M_ν has negligible effect, while variation of Y_{He} steepens the power law, degrading the constraints at the lowest value of τ_{sh} by about a factor of 2, and leaving the high τ_{sh} end unaffected. Accounting for interlopers (light dotted blue lines) degrades the constraint, most notably when simultaneously varying Y_{He} ; for low spectrometer-hours, the scaling of $\sigma(N_{\text{eff}})$ and τ_{sh} stays the same as the no-interloper case. However, the constraints begin to plateau when reaching $\tau_{\text{sh}} \sim \text{few} \times 10^8$. This is because increasing spectrometer-hours cannot compensate for the additional noise from interlopers. While constraints on N_{eff} are nearly unaffected by simultaneous variation of M_ν , varying Y_{He} degrades the constraints for both low and high values of τ_{sh} (about a factor of 2 for the latter).

2. When combining Planck and LIM (shown in dark blue lines in the top row), for low spectrometer-hours, the constraints are dominated by Planck. Nevertheless, the addition of LIM improves the Planck constraints by about a factor of 2 at the lowest value of τ_{sh} . Similar to LIM-only case, when accounting for interlopers, the constraints reach a plateau as we increase τ_{sh} . It is worth noting that, in combination with Planck, the impact of interlopers—in particular at high spectrometer-hours—is less significant compared to LIM-only constraints. When neglecting interlopers, enlarging the parameter space to vary M_ν or Y_{He} has negligible effect, while it degrades the constraints by about 30% for both cases, when interlopers are accounted for.
3. When considering LIM alone and neglecting interlopers, there exist multiple minima, as seen in the bottom row of panels. This arises from the fact that different line species, arising from separate redshifts with different brightnesses, require different survey depths (and correspondingly smaller f_{sky} for fixed spectrometer-hours) in order to achieve an optimal result. This apparent degeneracy in survey optimization is broken when moving to higher spectrometer-hours, as cosmic variance quickly becomes the dominant source of uncertainty for the low-redshift line species, and pushes the optimal design to deeper surveys (and correspondingly smaller sky areas) in order to probe the larger, higher-redshift cosmological volumes. This is the source of the large drop in optimal sky area seen in the top row of panels: as τ_{sh} increases, a survey focused on higher-redshift emission overtakes a lower-redshift survey as the optimal choice.
4. As demonstrated in the bottom two rows of panels in Figure 5, the constraining power of the survey is somewhat insensitive to the choice of f_{sky} , with a reasonably broad range (better than an order of magnitude in several cases) of near-optimal choices provided that you are above the threshold at which cosmic variance strongly dominates the measurement errors, particularly in the case where interlopers are included. This appears to be a consequence of the broad redshift coverage of the proposed survey, where competing effects of cosmic variance and instrument noise for low and high redshift, respectively, are relatively balanced in their impact on the constraining power.

We illustrate the information content of LIM at different redshifts in Figure 6, using an example survey with 1.45×10^8 spectrometer-hours.¹⁸ The contribution of interloper lines to the

¹⁸ This value of spectrometer-hours corresponds roughly to a survey using a filled focal plane on an SPT-like instrument, which could be fielded in the next decade.

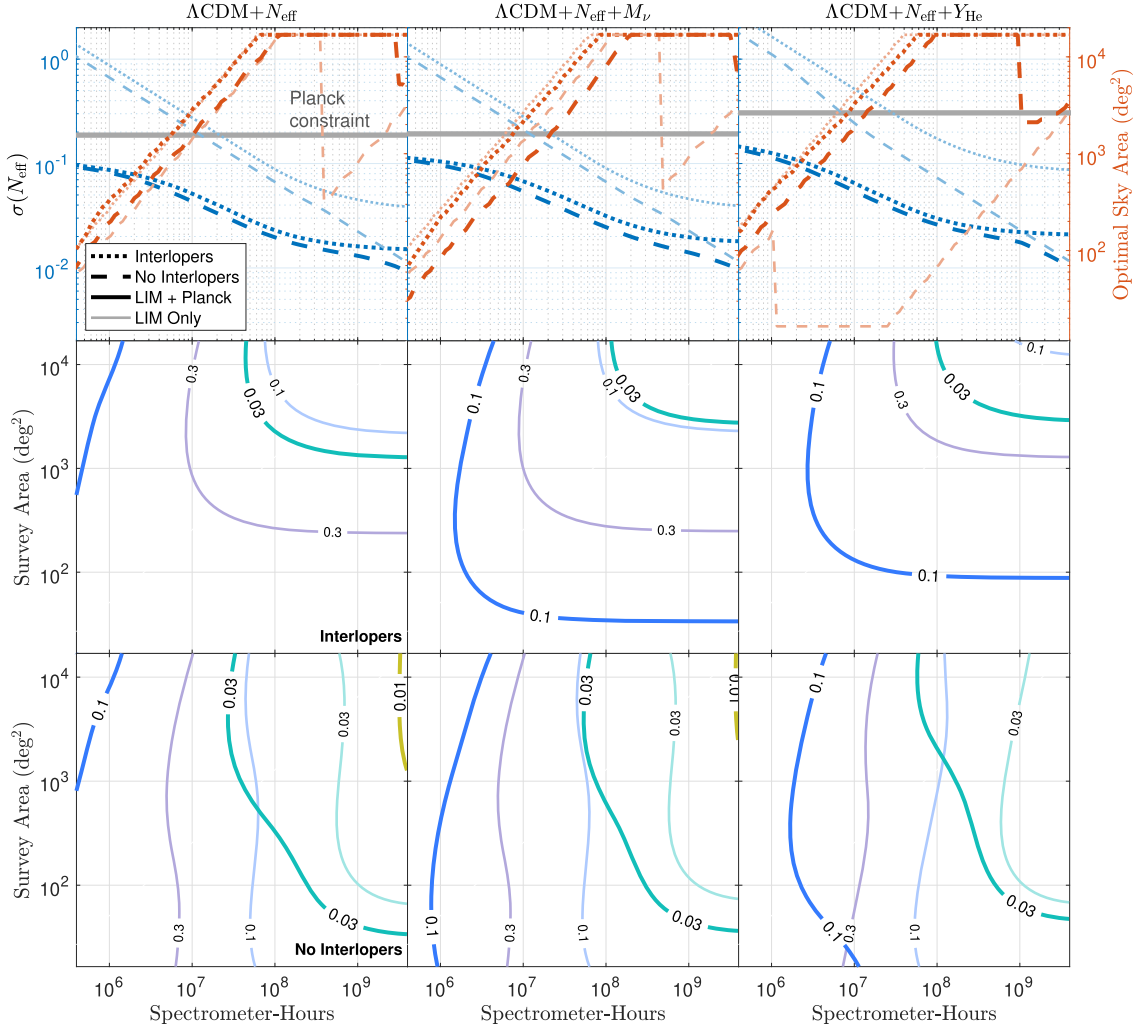


Figure 5. Optimized LIM surveys for probing light relics, from the combination of all six spectral lines. The columns from left to right correspond to varying only N_{eff} , or together with M_ν , or Y_{He} . *Top row:* 1σ marginalized constraints on N_{eff} as a function of spectrometer-hours (blue), and the corresponding sky coverage (red). The gray horizontal lines are Planck-only constraints. The lighter-shaded lines show the constraints from LIM-only, while the darker-shaded lines show the constraints from LIM + Planck. The dotted lines show the constraints with interlopers accounted for, and the dashed lines show the constraints when interloper emission is neglected. *Bottom two rows:* contours of constant 1σ errors on N_{eff} in the plane of survey area and spectrometer-hours, when interlopers are accounted for (middle) and when interlopers are neglected (bottom). The colors of different contours are matched to specific values for $\sigma(N_{\text{eff}})$ across all panels, to allow for ease of comparison. As is the case for the top row of panels, the lighter-shaded contours show the constraints from LIM-only, while the darker-shaded contours show the constraints from LIM+Planck.

noise (Equation (34)) is accounted for here, so these results are the worst-case interloper scenario. We show the 1σ marginalized constraints on N_{eff} as a function of maximum redshift included in the analysis, z_{max} , for LIM-only (left panel) and for Planck+LIM (middle panel). In the right panel, we show the $\sigma(N_{\text{eff}})$ per redshift bin from LIM-only, where z is the median redshift of the bin. Different colors show the constraints for various ΛCDM extensions. In the left and middle panels, we see that when holding M_ν constant (blue and green lines), the constraints nearly reach a plateau at $z \sim 2.5$. The reason for this saturation is that the main advantage of larger z_{max} for constraining N_{eff} is the increased mode count from a larger survey volume. However, at higher redshifts, the accessible volume increases more slowly than at lower redshifts. Therefore, the corresponding increase in volume provides little additional improvement to $\sigma(N_{\text{eff}})$. On the other hand, when varying neutrino mass, at $z < 4.5$, the orange line plateaus more slowly: higher z_{max} not only provides more modes but also probes the redshift-dependent imprint of the massive neutrinos on the power spectrum.

Furthermore, at $4.5 < z < 6$ there is a downward step feature, and $\sigma(N_{\text{eff}})$ reduces by $\sim 15\%$ for LIM-only and $\sim 20\%$ for Planck+LIM. This feature is due to the fact that at $z \geq 6$, in addition to the two highest CO rotational lines ($J = 5, 6$), we also detect the [C II] signal. Among these three lines, the constraining power lies predominantly with [C II] since it is the brightest at those redshifts (see Figures 1, 2), and the instrument considered in this work has the highest sensitivity to it. When considering the constraints per redshift bin (right panel of Figure 6), in all three cosmologies considered, $\sigma(N_{\text{eff}})$ improves at $z \sim 6$. However, in the cumulative constraints summed over all redshifts up to a z_{max} , the step feature is only seen when the neutrino mass is varied—here a longer redshift arm probes the redshift-dependence of the imprints of the neutrino mass. Finally, from the first plot on the left, we see that, summed over all redshift bins, extending the parameter space to include variation of Y_{He} degrades the LIM-only constraint on N_{eff} by about a factor of 2; leaving the sum of neutrino masses as a free parameter does not have a significant effect. When combined with the Planck data, the 2-parameter

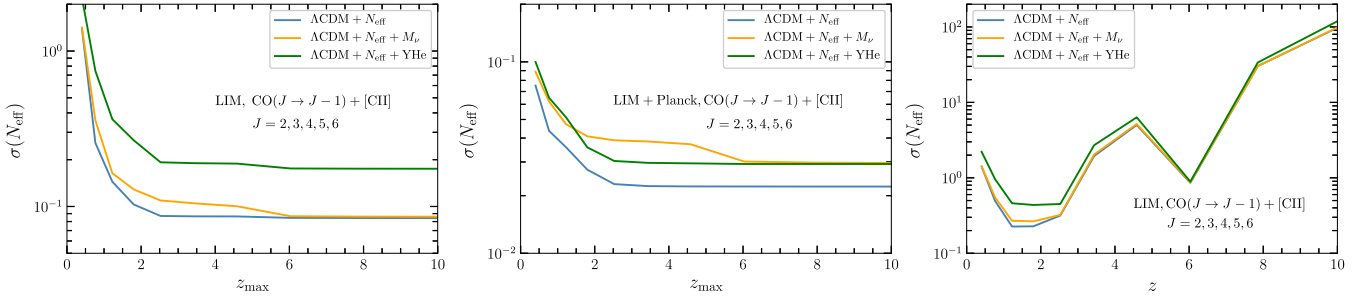


Figure 6. Redshift-dependence of 1σ marginalized constraints on N_{eff} , using the combination of all six spectral lines. The first two panels on the left show the constraints for LIM-only (left) and Planck+LIM (middle) as a function of maximum redshift, z_{max} , considered in the analysis (note the different vertical scales). The panel on the right shows the constraints per redshift bin, where z is the median redshift of the bin. Different colors show the constraints when only varying N_{eff} (blue), or co-varying it with M_ν (orange), or with Y_{He} (green). An optimized survey with 1.45×10^8 spectrometer-hours is assumed, and interloper lines are accounted for.

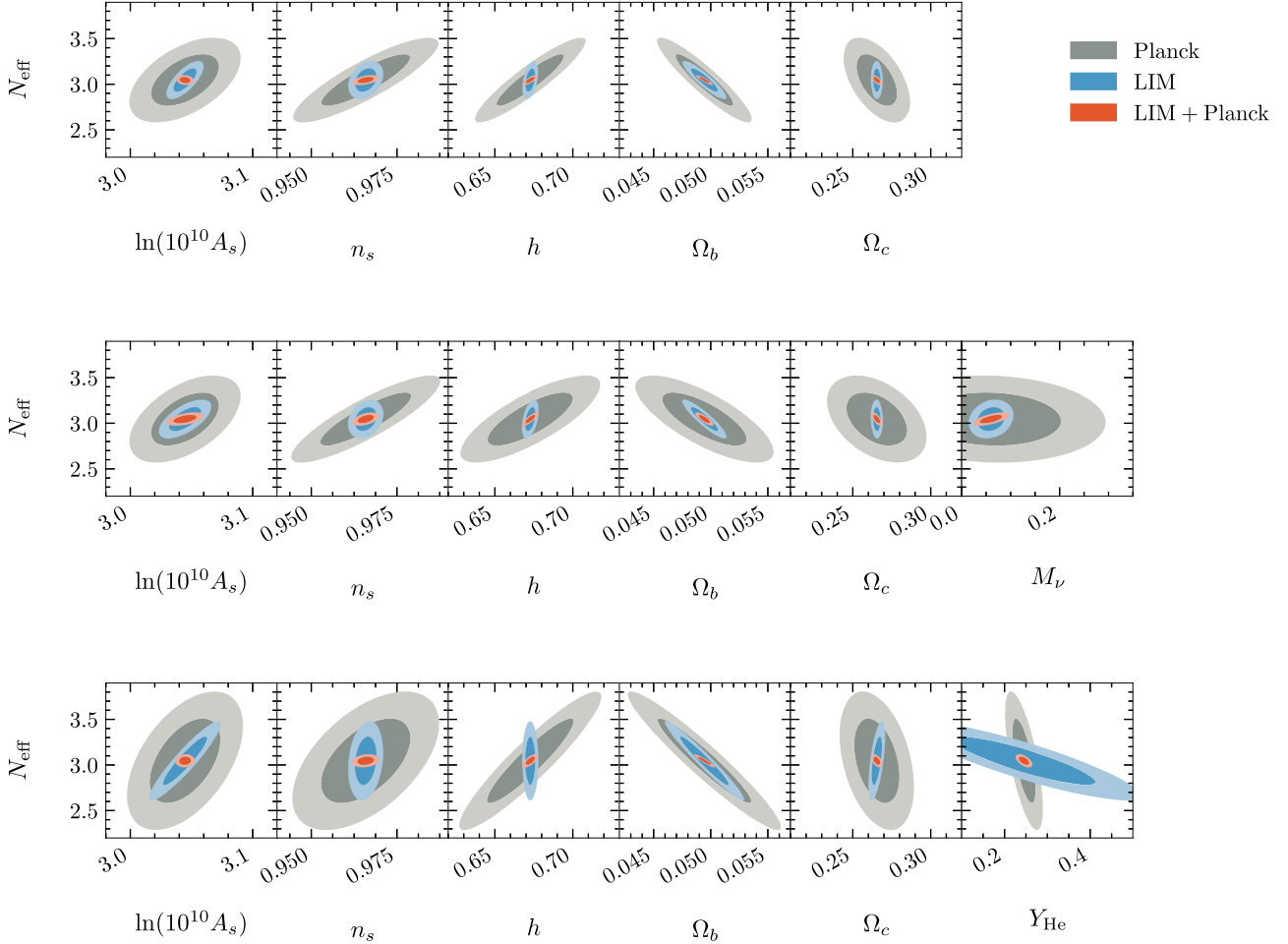


Figure 7. 2D marginalized constraints on N_{eff} in 1- and 2-parameter extensions of ΛCDM from combination of all spectral lines considered in this paper. The rows from top to bottom correspond to varying only N_{eff} (top), varying $N_{\text{eff}} + M_\nu$ (middle), and varying $N_{\text{eff}} + Y_{\text{He}}$ (bottom). Blue and gray contours correspond to constraints from Planck data and LIM individually, while the red contours are from combination of LIM and Planck. The LIM constraints correspond to an optimal survey with 1.45×10^8 spectrometer-hours, and interloper lines are accounted for.

extensions degrade the N_{eff} constraint similarly at high z_{max} , degrading by about a factor of 1.3 compared to the model with only N_{eff} free.

To highlight the importance of alleviating parameter degeneracies when combining LIM and CMB data, for an optimized survey with $\tau_{\text{sh}} = 1.45 \times 10^8$, in Figure 7, we show the 2D marginalized constraints on N_{eff} versus other cosmological parameters, with the Planck data in gray, LIM in blue, and their combination in red. The rows correspond to varying

only N_{eff} (top), or varying it together with M_ν (middle) or Y_{He} (bottom). The full triangle plots for the base model of $\Lambda\text{CDM} + N_{\text{eff}}$ are shown in Appendix B. In CMB data, various degeneracies weaken the constraint on N_{eff} . LIM alone provides significantly tighter constraints on all the parameters, except for Y_{He} , compared to Planck. Thanks to the difference in parameter degeneracy directions in CMB and LSS (most notably between N_{eff} and n_s , h , Ω_c , and Y_{He}), when combining LIM with Planck, the parameter constraints improve further.

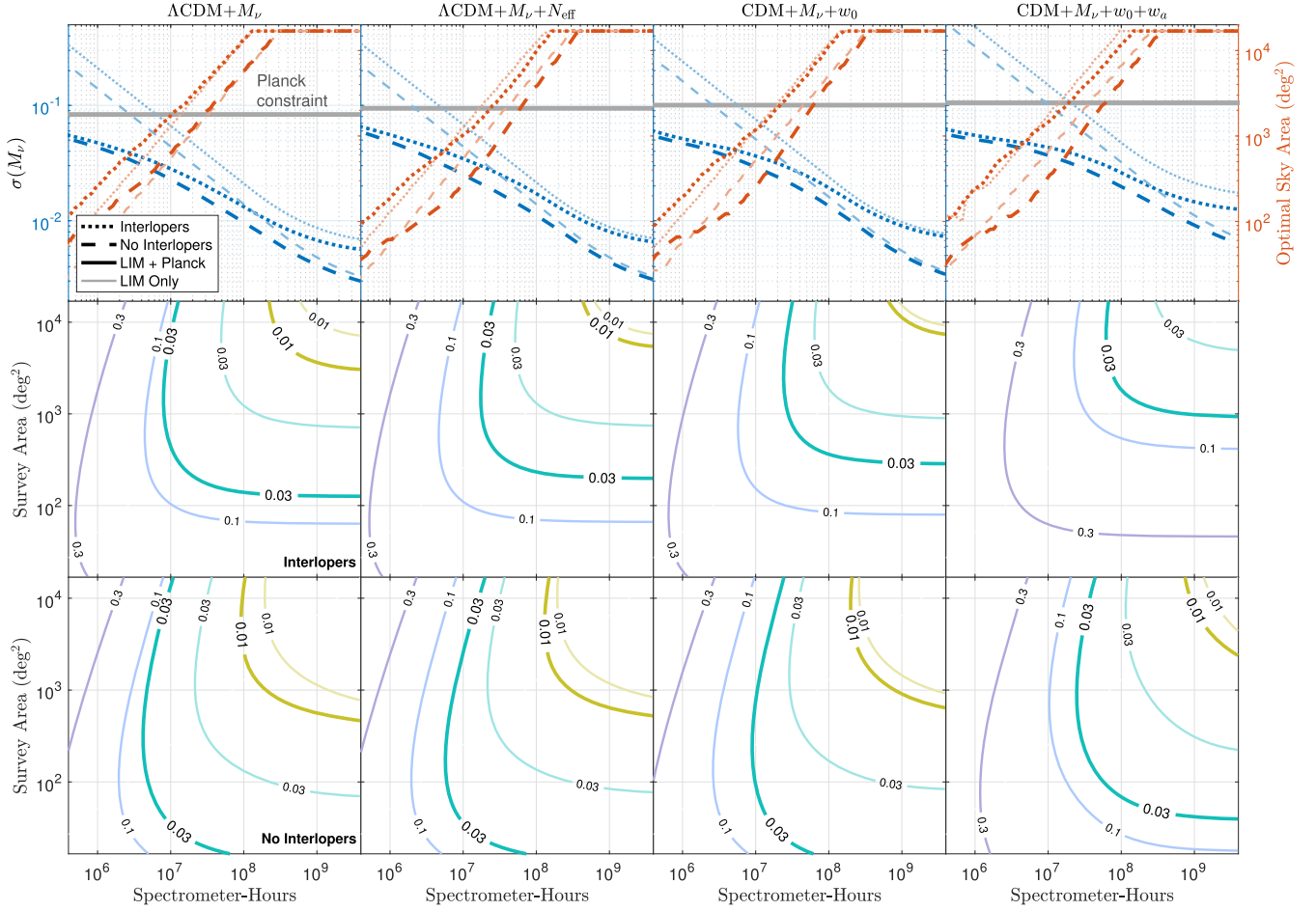


Figure 8. Optimized LIM surveys for probing the sum of neutrino masses, using the combination of all six spectral lines. The columns from left to right correspond to varying only M_ν , varying it together with N_{eff} , or w_0 , or $w_0 + w_a$. *Top row:* the blue lines show 1σ marginalized constraints on M_ν , as a function of spectrometer-hours. The red lines show the corresponding sky coverage. The gray horizontal lines show the Planck-only constraints. The lighter-shaded lines show the constraints from LIM-only, while the darker-shaded lines show the constraints from LIM+Planck. The dotted lines show the constraints with interlopers accounted for, and the dashed lines show the constraints when interloper emission is neglected. *Bottom two rows:* contours of constant 1σ errors on M_ν in the plane of survey area and spectrometer-hours, when interlopers are accounted for (middle) and when interlopers are neglected (bottom). The colors of different contours are matched to specific values for $\sigma(M_\nu)$ across all panels, to allow for ease of comparison. As is the case for the top row of panels, the lighter-shaded contours show the constraints from LIM-only, while the darker-shaded contours show the constraints from LIM+Planck.

The difference in degeneracy directions can be most clearly seen in the case of h and Y_{He} , and to a lesser extent for n_s and Ω_c .

6.2. Sum of Neutrino Masses

In the top row of Figure 8, as a function of spectrometer-hours, we show the best-achievable 1σ constraint on M_ν and the optimal sky area for that constraint. The bottom panels show the constant 1σ contours in the plane of survey area and spectrometer-hours. The columns from left to right show the constraints when varying only M_ν (first), varying it simultaneously with N_{eff} (second), w_0 (third), and $w_0 + w_a$ (fourth). The line styles and colors are the same as in Figure 5. The main observations from these plots can be summarized as follows:

1. The top row shows that when considering LIM alone and neglecting interlopers (dashed light blue lines), for all models considered, $\sigma(M_\nu)$ decreases nearly as a power law when increasing spectrometer-hours, τ_{sh} (the curves very slowly flatten at the highest end). Simultaneous variation of N_{eff} does not degrade the constraints. On the other hand, assuming dynamic DE and varying both w_0 and w_a

increases $\sigma(M_\nu)$ by a factor of ~ 2.5 ; assuming a constant EoS and varying only w_0 degrade the constraint only mildly (at most by $\sim 25\%$). Including interlopers as a source of noise (dotted light blue lines) degrades the constraint with a similar trend in all four cosmologies considered. For low values of spectrometer-hours, the scaling of $\sigma(M_\nu) - \tau_{\text{sh}}$ stays the same as in the no-interloper case. However, the constraints approach a plateau at $\tau_{\text{sh}} \sim 10^9$. As in the case of N_{eff} discussed previously, this is due to the interlopers starting to dominate the error budget.

2. The top row further shows that, for the combination of Planck+LIM with and without interlopers (dotted and dashed dark blue lines), constraints are dominated by Planck data at low values of τ_{sh} . Nevertheless, the addition of LIM improves the Planck constraints by $\sim 30\%$ when varying M_ν alone or together with N_{eff} , and $\sim 40\%$ when also varying the DE parameter. Including interlopers, the constraints approach a plateau as we increase τ_{sh} . Different from the case of N_{eff} , at the high end of spectrometer-hours, the LIM-only and Planck+LIM curves trace each other closely since LIM almost entirely dominates the constraining power.

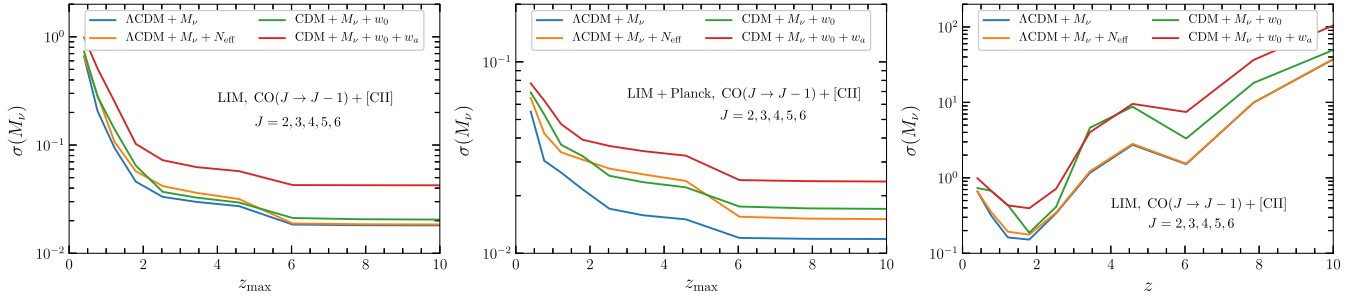


Figure 9. Redshift-dependence of 1σ marginalized constraints on M_ν (in unit of [eV]), from the combination of all six spectral lines. The first two plots on the left show the constraints for LIM-only (middle) and Planck+LIM (right) as a function of maximum redshift, z_{max} , while the panel on the right shows the constraints per redshift bin, where z is the median redshift of the bin. Different colors correspond to only varying M_ν (blue), or co-varying it with N_{eff} (orange), with w_0 (green), or with $w_0 + w_a$ (red). An optimized survey with 1.45×10^8 spectrometer-hours is assumed, and interloper lines are accounted for.

- Generally, we find that the optimal f_{sky} increases roughly as $\tau_{\text{sh}}^{2/3}$, which can be understood as maintaining the balance between uncertainties driven by cosmic variance (which roughly decreases as $f_{\text{sky}}^{-0.5}$) and instrument noise (which at fixed volume, decreases inversely with τ_{sh}). At the low end of spectrometer-hours ($\lesssim 10^6$) for Planck+LIM, the slope is shallower, due to the Planck priors that provide the bulk of the constraining power for $\sigma(M_\nu)$. The primary additive strength is in breaking the degeneracies in the Planck data.
- Similar to the case with N_{eff} , the constraining power of a given survey is somewhat insensitive to the choice of f_{sky} , provided that you are above the threshold at which cosmic variance strongly dominates the measurement errors.

In the left and middle panels of Figure 9, we plot $\sigma(M_\nu)$ as a function of z_{max} from LIM alone and from its combination with Planck. In the right panel, we show $\sigma(M_\nu)$ per redshift bin, with z being the median redshift of the bin. The survey specifications are the same as in Figure 6, and constraints for various extensions of ΛCDM are shown in different colors. When considering LIM alone, enlarging the parameter space does not degrade the constraints dramatically, except for when assuming redshift-dependent DE and varying both w_0 and w_a . For the combined LIM and Planck data, however, varying additional parameters increases $\sigma(M_\nu)$ more considerably. Again, we see the same downward step features as in Figure 6 at $4.5 < z < 6$ as a result of the additional [C II] signal at $z \geq 6$. For $\Lambda\text{CDM} + M_\nu$ cosmology, the 1σ errors on M_ν reduce by $\sim 30\%$ for LIM alone and by $\sim 20\%$ for Planck+LIM. The plateau at $z > 6$ is due to larger instrument and interloper noise.

We note that at $z < 4.5$, compared to $\sigma(N_{\text{eff}})$ in Figure 6, the constraints approach a plateau more slowly. As discussed before, going to higher z_{max} not only provides more modes but also allows for probing the redshift-dependent imprint of the massive neutrinos on the power spectrum. The per-bin constraints shown in the right panel of Figure 9 indicate that the improvement at $z \sim 6$ (seen in the cumulative plots on the right) is driven not only by an additional [C II] signal at $z \sim 6$ but also by having a long redshift arm to probe the redshift evolution of the suppression of the matter power spectrum and growth rate of the structure.

Finally, in Figure 10, we show the 2D marginalized constraints on M_ν for an optimized survey with 1.45×10^8 spectrometer-hours, for Planck (in gray), LIM (in blue), and their combination (in red). The rows from top to bottom correspond to varying only M_ν (first), or co-varying it with N_{eff} (second), w_0 (third), and $w_0 + w_a$ (fourth). The full triangle plots for the base model of

$\Lambda\text{CDM} + M_\nu$ are shown in Appendix B. Again, LIM data by itself significantly improves the constraints on all cosmological parameters. Apart from neutrino mass and ΛCDM parameters, LIM data provide very tight constraints on the DE EoS (see Table 4 for 1σ constraints). Additionally, the combination with Planck tightens constraints further by breaking parameter degeneracies thanks to the different degeneracy directions for CMB and LSS observables. Enlarging the parameter space affects the LIM constraints much less significantly than CMB (temperature+polarization) data. This is most notable when including the variation of DE, for which CMB primary anisotropies largely lose their constraining power.

7. Conclusions

In this work, we have forecasted the constraining power of next-generation ground-based millimeter-wave LIM experiments on N_{eff} and M_ν . Over a wide range of experimental sensitivities, for a variety of extensions to ΛCDM , we used the Fisher formalism to determine the tightest possible constraints and the optimal survey area, evaluating both the best- and worst-case interloper line mitigation scenarios. We considered a range of experimental sensitivities, as summarized in Table 2, along with a rough estimate for the time at which such surveys could start, driven by the anticipated increase in density of on-chip spectrometers.

One of the primary advantages of millimeter-wave LIM is cost-effectiveness, especially compared to contemporary optical galaxy surveys and space missions. While the detector technology is still being developed, millimeter-wave spectrometers draw from a long heritage of CMB experience in mass-producing densely packed, background-limited detectors. Completing the research and development for compact millimeter-wave spectrometers and outfitting an existing instrument such as the SPT with a full complement of $R = 300$ spectrometers would enable a LIM survey of the order $\sim 10^8$ spectrometer-hours to be completed. Such a survey could be deployed by the end of the decade, at a significantly lower cost than experiments such as CMB-S4 or EUCLID.

We have shown that with a conservative assumption of no removal of line interloper noise, an optimized survey of $\sim 10^8$ spectrometer-hours covering 40% of the sky, combined with Planck, can constrain the effective number of light relics at the level of $\sigma(N_{\text{eff}}) \simeq 0.023$, providing a 1.2σ exclusion of the minimal thermal abundance. For the sum of neutrino masses, such a survey would reach the precision of $\sigma(M_\nu) \simeq 13 \text{ meV}$, providing $\sim 5\sigma$ (8σ) detection of the minimum neutrino mass in

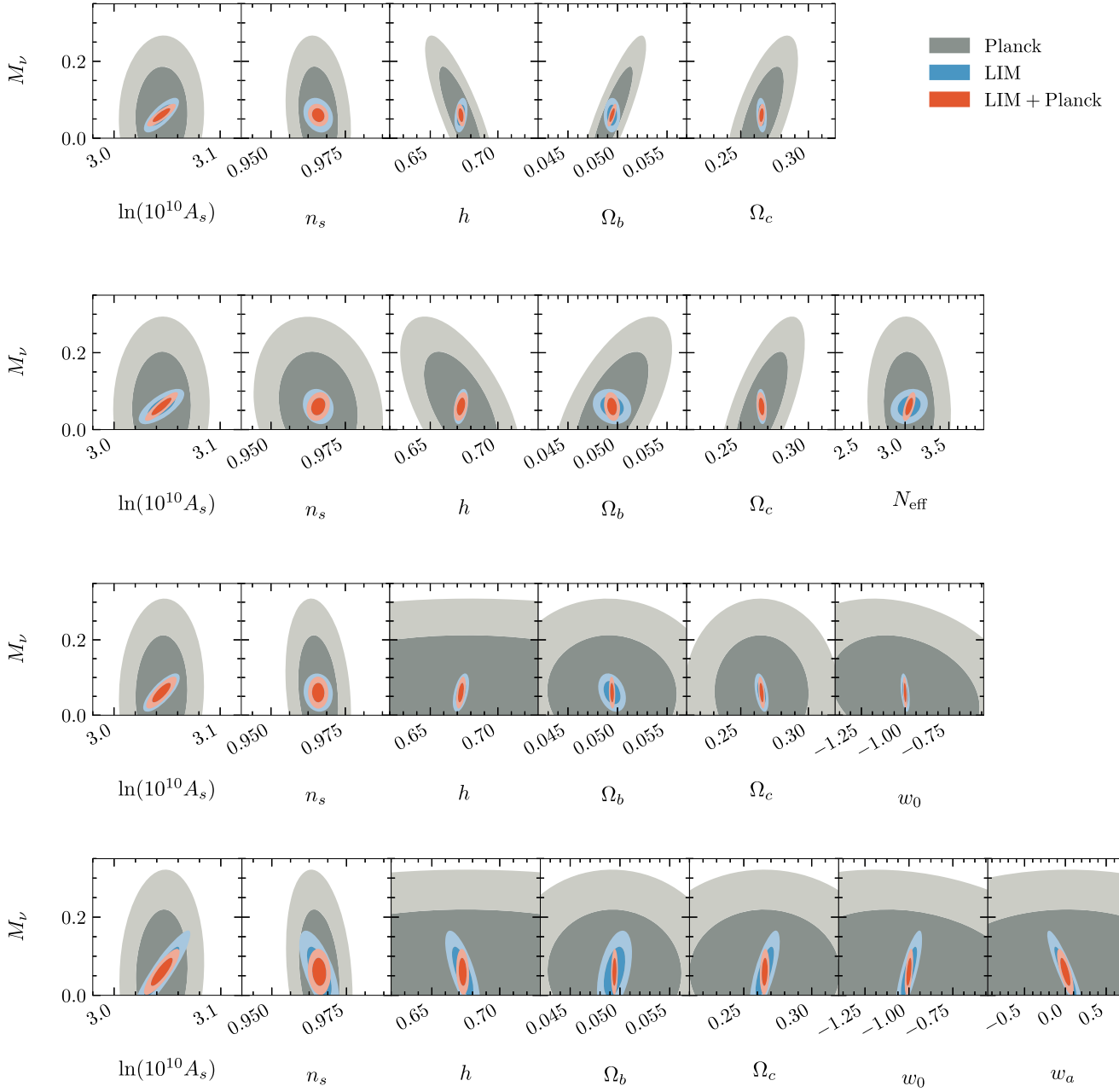


Figure 10. 2D marginalized constraints on M_ν from combination of all of the spectral lines considered in this paper. Rows from top to bottom correspond to varying only M_ν (first row), varying it together with N_{eff} (second row), with w_0 (third row), or with $w_0 + w_a$ (fourth row). Color coding and LIM specifications are the same as Figure 7.

the normal (inverted) hierarchy. In comparison to the constraints from CMB-S4 and EUCLID—the latter shown in further detail in Appendix B—such a survey would provide meaningful and complementary contributions to the constraints on M_ν and N_{eff} .

We show results both for LIM alone and combined with Planck to illustrate parameter degeneracies that LIM helps to alleviate. In particular, we note that even more modest surveys of 10^6 – 10^7 spectrometer-hours can significantly improve constraints on N_{eff} and M_ν by breaking degeneracies in the Planck data. As discussed earlier, more realistic modeling will affect our constraints on cosmological parameters. This will include extending the linear model of the line power spectrum to include one-loop corrections, and marginalizing over additional line biases introduced at the one-loop level (Sailer et al. 2021). We leave the quantification of these effects to future work.

While we have only considered the information content of the line power spectrum in combination with Planck, exploiting higher-order statistics and synergies between LIM and future CMB and galaxy surveys would not only improve the forecasted constraints but also offer a means to overcome degeneracies with nuisance astrophysical parameters. Furthermore, such information could improve the mitigation of systematics and foregrounds. We leave further studies in these directions to future work.

While our focus in this paper has been on constraining neutrino properties, the discussed LIM surveys offer unique opportunities for a multitude of other science goals. Our results show that the considered surveys can provide exquisite constraints on Λ CDM parameters and the DE EoS (see Table 4). The combination of Planck+LIM would achieve $\sigma(w_0) = 0.0051$ and $\{\sigma(w_0) \simeq 0.0098, \sigma(w_a) \simeq 0.041\}$, assuming $\sim 10^8$

Table 2
Future Survey Capabilities

Spec-hours	Example	Deployment Timescale	$\sigma(M_\nu)$ [eV]		$\sigma(N_{\text{eff}})$	
			Int.	No Int.	Int.	No Int.
10^5	TIME	Now	0.69 (0.066)	0.48 (0.061)	2.8 (0.11)	2.0 (0.10)
10^6	TIME-EXT	3 yr	0.21 (0.047)	0.14 (0.043)	0.87 (0.087)	0.67 (0.082)
10^7	SPT-like, 1 tube	4 yr	0.066 (0.028)	0.044 (0.023)	0.27 (0.051)	0.21 (0.043)
10^8	SPT-like, 7 tubes	8 yr	0.021 (0.013)	0.014 (0.0097)	0.088 (0.023)	0.0674 (0.020)
10^9	CMB-S4-like, 85 tubes	12 yr	0.0087 (0.0068)	0.0048 (0.0041)	0.045 (0.016)	0.022 (0.013)

Note. Potential stages of future millimeter-wave LIM experiments and corresponding neutrino constraints. Values provided are for LIM-only (with Planck+LIM in parentheses), for the best- and worst-case interloper scenarios. For each stage of the experiments, we provide an approximate example of the class of instrument required for such a survey. For future instruments, an optics tube is assumed to hold a focal plane of ~ 400 on-chip spectrometers observing from 80 to 310 GHz. Future surveys are assumed to run for multiple years, observing for several thousands of hours per year. The timescale is a rough estimate to when such a survey could begin operations.

spectrometer-hours. The wide redshift range probed by such surveys would uniquely constrain the redshift-dependence of the expansion history, DE models, and modifications to gravity (see, e.g., Karkare & Bird 2018; Bernal et al. 2019 for existing forecasts for non-21 cm lines; and Lorenz et al. 2017; Sailer et al. 2021 for 21 cm). Furthermore, the large sky coverage and wide redshift range of such surveys make them particularly well-suited to probe primordial non-Gaussianity (see, e.g., Moradinezhad Dizgah et al. 2019; Moradinezhad Dizgah & Keating 2019; Liu & Breysse 2021; Viljoen et al. 2021). This wide range of potential science targets and the unique opportunity to probe fundamental physics are strong motivations for developing the instrumental and observational techniques needed for high-sensitivity millimeter-wave LIM surveys.

An important caveat to the above is that, while quite mature for CMB and galaxy surveys, instrument hardware and analysis methods for LIM surveys are still in a relatively nascent state, with the field primarily focused on pathfinder instruments and initial detections. Millimeter-wave LIM instruments have an advantage of a long heritage of CMB experiments, focused on similar wavelengths with well-developed sites and observation strategies, which in addition to reducing costs can also help mitigate the impact of systematics—a significant challenge for observations at longer wavelengths (e.g., 21 cm cosmology; Nasirudin et al. 2020). While pathfinder experiments will help to pave the path forward, the success of such large-scale surveys will require continued technical development, both in instrumentation and analysis tools.

Should such efforts prove successful, surveys even larger than our nominal 10^8 spectrometer-hours would have significant additive value. At the maximum survey scale considered here

(4×10^9 spectrometer-hours), in combination with Planck, one could constrain $\sigma(N_{\text{eff}}) \simeq 0.015$ and $\sigma(M_\nu) \simeq 5.6$ meV. While this would be a significant undertaking, these improvements suggest that such a survey is worth further consideration. At such large numbers of spectrometer-hours, the constraints become primarily limited by cosmic variance, so that sites that can observe a larger sky fraction become highly desirable. A space-based mission would be capable of measuring the largest possible sky area, and our analysis suggests that constraints on neutrinos—along with other cosmological parameters—may be strong science motivators for the potential futuristic space-based LIM surveys now being discussed (e.g., Delabrouille et al. 2019; Silva et al. 2021).

It is our pleasure to thank Emanuele Castorina for many insightful discussions as well as his feedback on the draft. We also thank Amol Upadhye, Enea Di Dio, and Steen Hannestad for helpful discussions, and Adam Anderson and Clarence Chang for their detailed comments on the draft of this paper. Finally, we thank Ana Diaz for collaborations at the very early stages of this work. A.M.D. is supported by the SNSF project “The Non-Gaussian Universe and Cosmological Symmetries,” project number: 200020-178787. A.M.D. also acknowledges partial support from Tomalla Foundation for Gravity.

Appendix A

Redshift Binning and Instrument Noise

In Table 3, we show the value of P_N used for each redshift bin, provided the instrument and atmospheric parameters in Section 4, for our smallest survey area (16.5 deg^2) and

Table 3
Estimated Per-mode Instrument Noise

Line Species	Median Redshift (z)									
	0.40	0.77	1.2	1.8	2.5	3.4	4.6	6.0	7.9	10.1
CO(2-1)	2.8	3.2	3.7	3.7
CO(3-2)	2.4	3.6	3.2	3.8	4.2
CO(4-3)	...	3.0	3.3	3.6	3.7	4.1	4.4
CO(5-4)	3.4	3.5	3.8	3.7	4.1	4.5
CO(6-5)	3.3	4.2	3.6	4.1	4.3
[C II]	3.7	3.9	3.8

Note. Values are given in units of $\log_{10}[\mu\text{K}^2 (h/\text{Mpc})^3]$, covering 16.5 deg^2 , with 2×10^5 spectrometer-hours, following the instrument parameters and weather conditions provided in Section 4. Redshift bins are spaced such that they are 0.1 dex wide, to account for instrument noise variation and redshift evolution of the line-emitting population of sources.

minimum integration time (2×10^5 spectrometer-hours). For surveys of different times and integration times, we use Equation (16) to estimate the noise, which dictates that $P_N \propto \Omega_s \tau_{sh}^{-1}$.

Appendix B Comparison with EUCLID

In this appendix, we show the forecasted parameter constraints for the models described in Table 1 from the EUCLID spectroscopic sample combined with the Planck temperature and polarization data. We also show the results from LIM-only and its combination with Planck. For EUCLID, we use the specifications and given in Table 3 of the recent official EUCLID forecast paper (Blanchard et al. 2020). The full survey covers an area of 15,000 deg², observing H α emitters in the redshift range of $0.9 < z < 1.8$, and binning the data in four redshift bins. We refer to the aforementioned paper for the expected values of shot noise and linear biases.

Analogous to line intensity power spectrum, we model the galaxy power spectrum assuming linear perturbation theory, and include the RSD and AP effect. Therefore, we have

$$P_g(k, \mu, z) = \frac{H_{\text{true}}(z)}{H_{\text{ref}}(z)} \left[\frac{D_{A,\text{ref}}(z)}{D_{A,\text{true}}(z)} \right]^2 \times \exp \left(-\frac{k_{\text{true}}^2 \mu_{\text{true}}^2 \sigma_v^2}{H^2(z)} \right) \times [1 + \mu_{\text{true}}^2 \beta(k_{\text{true}}, z)]^2 b_g^2(z) P_0(k_{\text{true}}, z). \quad (\text{B1})$$

For the spectroscopic galaxy sample, the σ_z in Equation (12) represents the spectroscopic redshift error, which for EUCLID is given by $\sigma_z = 0.001(1+z)$. For each redshift bin, we set the value of k_{max} as described in Section 5.

In Table 4, we show the 1σ constraints from the Planck data, Planck+EUCLID, and Planck+LIM. In the baseline cosmologies (1-parameter extensions to Λ CDM), our constraints from the combination of EUCLID and Planck are in broad agreement with the values reported in Obuljen et al. (2018) and Sprenger et al. (2019). To demonstrate the parameter degeneracies, in Figure 11, we show the 2D marginalized errors for the full set of cosmological parameters when considering Planck (gray), LIM (blue) data alone and combined (red), while in Figure 12 we show the corresponding plots for EUCLID. In each figure, the top plot shows the constraints for Λ CDM + N_{eff} , while the bottom is for Λ CDM + M_ν . Note that the

Table 4

1σ Marginalized Constraints on Cosmological Parameters from Planck Data Alone, Planck Combined with EUCLID (Galaxy Clustering), and Planck Combined with LIM with $\sim 10^8$ Spectrometer-hours

Λ CDM + N_{eff}			
Parameters	Planck	+EUCLID	+LIM
$\ln(10^{10}A_s)$	0.018	0.0035	0.0029
n_s	0.0085	0.0033	0.0016
h	0.014	0.0056	0.0019

Table 4
(Continued)

Λ CDM + N_{eff}			
Parameters	Planck	+EUCLID	+LIM
Ω_b	0.0017	0.00065	0.00030
Ω_c	0.0086	0.0031	0.0014
N_{eff}	0.187	0.073	0.023
Λ CDM + M_ν			
Parameters	Planck	+EUCLID	+LIM
$\ln(10^{10}A_s)$	0.015	0.012	0.0055
n_s	0.0044	0.0029	0.0014
h	0.011	0.0024	0.0013
Ω_b	0.0014	0.00035	0.00018
Ω_c	0.011	0.0024	0.0011
M_ν [eV]	0.083	0.031	0.013
Λ CDM + N_{eff} + M_ν			
Parameters	Planck	+EUCLID	+LIM
$\ln(10^{10}A_s)$	0.018	0.013	0.0063
n_s	0.0088	0.0037	0.0016
h	0.018	0.0056	0.0021
Ω_b	0.0022	0.00067	0.00033
Ω_c	0.012	0.0031	0.0014
M_ν [eV]	0.094	0.035	0.015
N_{eff}	0.192	0.081	0.030
Λ CDM + N_{eff} + Y_{He}			
Parameters	Planck	+EUCLID	+LIM
$\ln(10^{10}A_s)$	0.019	0.0040	0.0032
n_s	0.0086	0.0037	0.0016
h	0.018	0.0059	0.0019
Ω_b	0.0027	0.00089	0.00038
Ω_c	0.0096	0.0031	0.0014
Y_{He}	0.018	0.012	0.0079
N_{eff}	0.30	0.10	0.029
Λ CDM + M_ν + w_0			
Parameters	Planck	+EUCLID	+LIM
$\ln(10^{10}A_s)$	0.016	0.014	0.0058
n_s	0.0055	0.0034	0.0014
h	0.091	0.0058	0.0014
Ω_b	0.0054	0.00098	0.00013
Ω_c	0.023	0.0034	0.0010
w_0	0.28	0.018	0.0051
M_ν [eV]	0.10	0.043	0.017
Λ CDM + M_ν + w_0 + w_a			
Parameters	Planck	+EUCLID	+LIM
$\ln(10^{10}A_s)$	0.016	0.013	0.0057
n_s	0.0045	0.0029	0.0015
h	0.097	0.0054	0.0019
Ω_b	0.0044	0.00026	0.00014
Ω_c	0.037	0.0026	0.0014
w_0	0.42	0.027	0.0098
w_a	1.0	0.096	0.041
M_ν [eV]	0.11	0.045	0.024

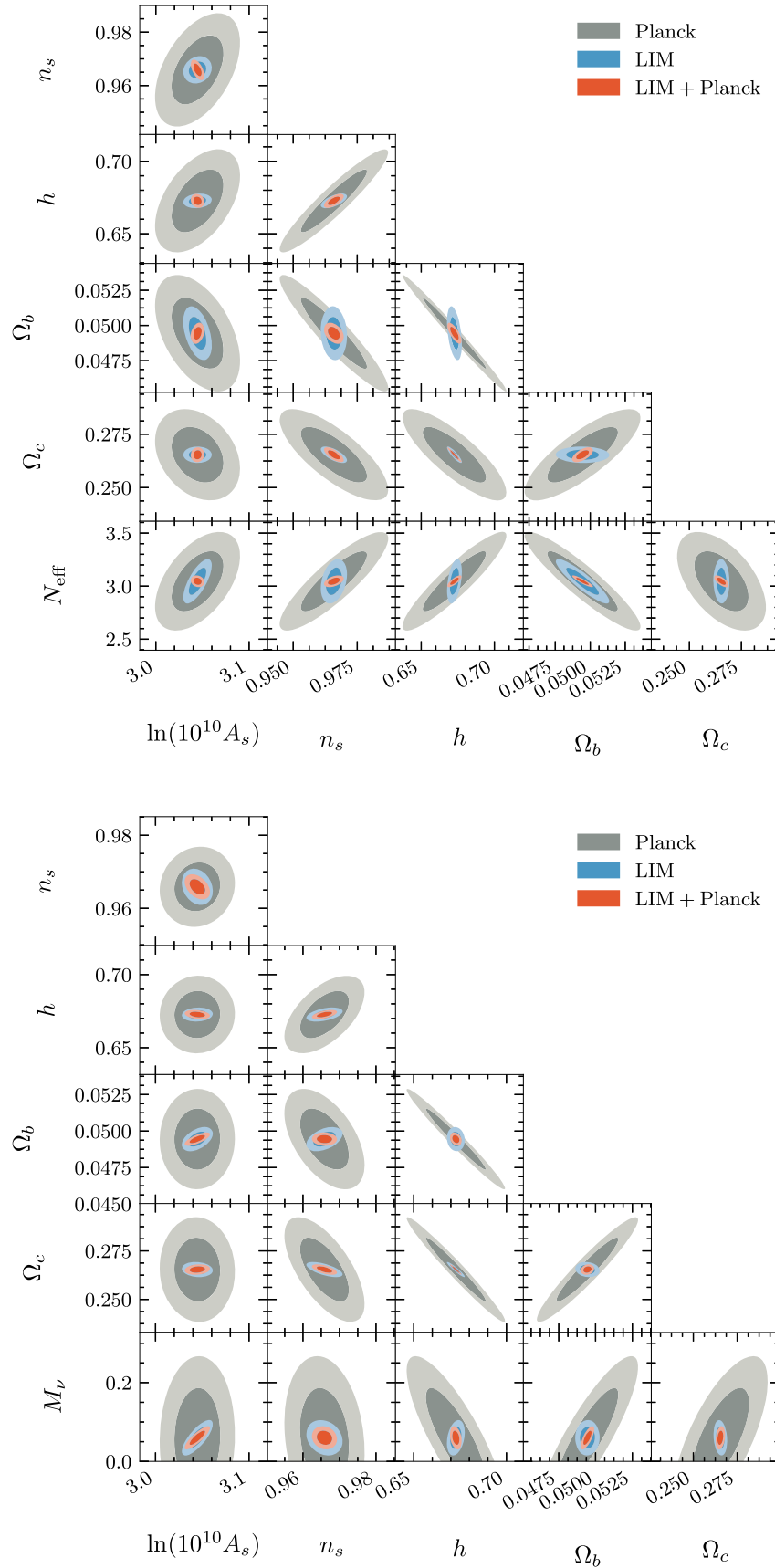


Figure 11. 2D marginalized constraints on cosmological parameters for $\Lambda\text{CDM} + N_{\text{eff}}$ (top) and $\Lambda\text{CDM} + M_\nu$ model (bottom), from Planck and LIM data alone and combined. LIM constraints correspond to an optimal survey with 10^8 spectrometer-hours, and interloper lines are accounted for.

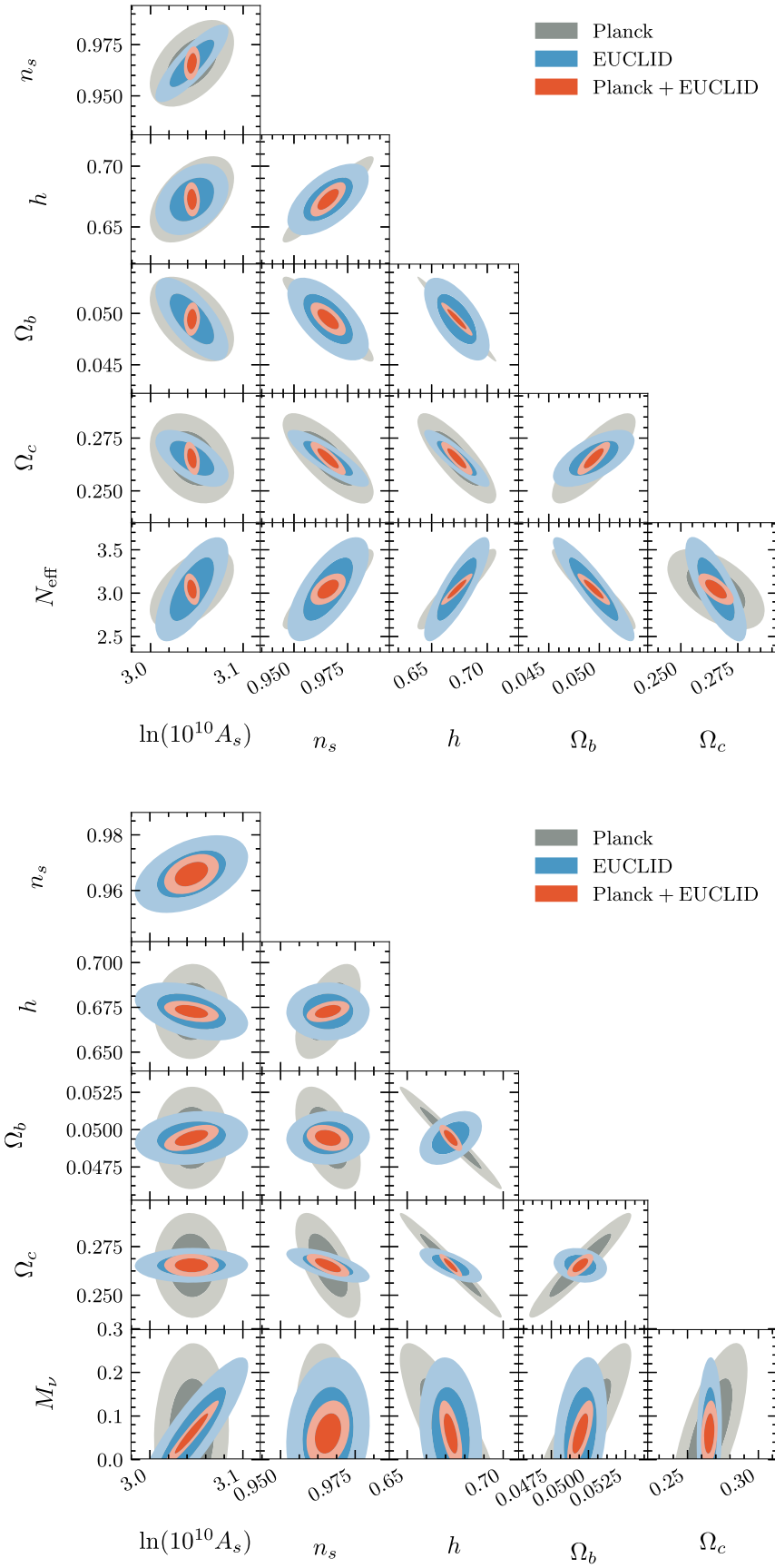


Figure 12. 2D marginalized constraints on cosmological parameters for Λ CDM + N_{eff} (top) and Λ CDM + M_ν model (bottom) from Planck (gray) and EUCLID (blue) data alone and combined (red).

combination of galaxy lensing and clustering measurements from EUCLID will provide tighter constraints on neutrino properties compared to those reported here using spectroscopic clustering only (see, e.g., Sprenger et al. 2019).

ORCID iDs

Azadeh Moradinezhad Dizgah  <https://orcid.org/0000-0001-8841-9989>

Garrett K. Keating  <https://orcid.org/0000-0002-3490-146X>

Kirit S. Karkare  <https://orcid.org/0000-0002-5215-6993>

Shouvik Roy Choudhury  <https://orcid.org/0000-0002-5589-3454>

References

- Abazajian, K., Addison, G., Adshead, P., et al. 2019, arXiv:1907.04473
- Abazajian, K. N., Acero, M. A., Agarwalla, S. K., et al. 2012, arXiv:1204.5379
- Abazajian, K. N., Adshead, P., Ahmed, Z., et al. 2016, arXiv:1610.02743
- Abe, K., Aihara, H., Aimi, A., et al. 2018b, arXiv:1805.04163
- Abe, K., Akutsu, R., Ali, A., et al. 2018c, *PhRvL*, **121**, 171802
- Abe, K., Bronner, C., Haga, Y., et al. 2018a, *PhRvD*, **97**, 072001
- Abi, B., Acciarri, R., Acero, M. A., et al. 2020, *EPJC*, **80**, 978
- Acero, M. A., Adamson, P., Aliaga, L., et al. 2019, *PhRvL*, **123**, 151803
- Ade, P., Aguirre, J., Ahmed, Z., et al. 2019, *JCAP*, **02**, 056
- Aghanim, N., Akrami, Y., Ashdown, M., et al. 2020, *A&A*, **641**, A6
- Allison, R., Caucal, P., Calabrese, E., Dunkley, J., & Louis, T. 2015, *PhRvD*, **92**, 123535
- Anderson, A. J., Ade, P. A. R., Ahmed, Z., et al. 2019, *JLTP*, **199**, 320
- Archidiacono, M., Brinckmann, T., Lesgourgues, J., & Poulin, V. 2017, *JCAP*, **02**, 052
- Archidiacono, M., Hannestad, S., Hansen, R. S., & Tram, T. 2015, *PhRvD*, **91**, 065021
- Archidiacono, M., Hannestad, S., & Lesgourgues, J. 2020, *JCAP*, **09**, 021
- Bashinsky, S., & Seljak, U. 2004, *PhRvD*, **69**, 083002
- Baumann, D., Green, D., & Wallisch, B. 2016, *PhRvL*, **117**, 171301
- Baumann, D., Green, D., & Wallisch, B. 2018, *JCAP*, **08**, 029
- Baumann, D., Green, D., & Zaldarriaga, M. 2017, *JCAP*, **1711**, 007
- Baumann, D. D., Beutler, F., Flauger, R., et al. 2019, *NatPh*, **15**, 465
- Bayer, A. E., Banerjee, A., & Seljak, U. 2021a, arXiv:2108.04215
- Bayer, A. E., Villaescusa-Navarro, F., Massara, E., et al. 2021b, *ApJ*, **919**, 24
- Behroozi, P. S., Wechsler, R. H., & Conroy, C. 2013, *ApJL*, **762**, L31
- Bernal, J. L., Breyse, P. C., & Kovetz, E. D. 2019, *PhRvL*, **123**, 251301
- Bernal, J. L., Caputo, A., & Kamionkowski, M. 2021, *PhRvD*, **103**, 063523
- Bernal, J. L., Caputo, A., Villaescusa-Navarro, F., & Kamionkowski, M. 2021, *PhRvL*, **127**, 131102
- Bird, S., Viel, M., & Haehnelt, M. G. 2012, *MNRAS*, **420**, 2551
- Biswas, R., Heitmann, K., Habib, S., et al. 2019, arXiv:1901.10690
- Blanchard, A., Camera, S., Carbone, C., et al. 2020, *A&A*, **642**, A191
- Blas, D., Lesgourgues, J., & Tram, T. 2011, *JCAP*, **07**, 034
- Bond, J. R., Efstathiou, G., & Silk, J. 1980, *PhRvL*, **45**, 1980
- Boyle, A., & Komatsu, E. 2018, *JCAP*, **2018**, 035
- Boyle, A., & Schmidt, F. 2021, *JCAP*, **2021**, 022
- Brandbyge, J., Hannestad, S., Haugbølle, T., & Thomsen, B. 2008, *JCAP*, **08**, 020
- Breyse, P. C., Kovetz, E. D., & Kamionkowski, M. 2014, *MNRAS*, **443**, 3506
- Breyse, P. C., Kovetz, E. D., & Kamionkowski, M. 2015, *MNRAS*, **452**, 3408
- Brinckmann, T., Hooper, D. C., Archidiacono, M., Lesgourgues, J., & Sprenger, T. 2019, *JCAP*, **01**, 059
- Brust, C., Kaplan, D. E., & Walters, M. T. 2013, *JHEP*, **12**, 058
- Carilli, C., & Walter, F. 2013, *ARA&A*, **51**, 105
- Castorina, E., Carbone, C., Bel, J., Sefusatti, E., & Dolag, K. 2015, *JCAP*, **07**, 043
- Castorina, E., Sefusatti, E., Sheth, R. K., Villaescusa-Navarro, F., & Viel, M. 2014, *JCAP*, **02**, 049
- Castorina, E., & White, M. 2019, *JCAP*, **06**, 025
- Cataldo, G., Moseley, S. H., Hsieh, W., et al. 2012, AAS Meeting Abstracts, **220**, 122.07
- Chacko, Z., Cui, Y., Hong, S., & Okui, T. 2015, *PhRvD*, **92**, 055033
- Chen, J. Z., Upadhye, A., & Wong, Y. Y. 2021a, *JCAP*, **03**, 065
- Chen, S.-F., Castorina, E., White, M., & Slosar, A. 2019, *JCAP*, **07**, 023
- Chen, S.-F., Lee, H., & Dvorkin, C. 2021b, *JCAP*, **05**, 030
- Cheng, Y.-T., Chang, T.-C., Bock, J., Bradford, C. M., & Cooray, A. 2016, *ApJ*, **832**, 165
- Cheng, Y.-T., Chang, T.-C., & Bock, J. J. 2020, *ApJ*, **901**, 142
- Chevallier, M., & Polarski, D. 2001, *IMPD*, **10**, 213
- Chudaykin, A., & Ivanov, M. M. 2019, *JCAP*, **11**, 034
- Creque-Sarbinowski, C., & Kamionkowski, M. 2018, *PhRvD*, **98**, 063524
- Crites, A. T., Bock, J. J., Bradford, C. M., et al. 2014, *Proc. SPIE*, **9153**, 9153
- De Looze, I., Cormier, D., Leboutteiller, V., et al. 2014, *A&A*, **568**, A62
- de Salas, P. F., Forero, D. V., Ternes, C. A., Tortola, M., & Valle, J. W. F. 2018, *PhLB*, **782**, 633
- de Salas, P. F., & Pastor, S. 2016, *JCAP*, **07**, 051
- Delabrouille, J., Abitbol, M. H., Aghanim, N., et al. 2019, arXiv:1909.01591
- DePorzio, N., Xu, W. L., Muñoz, J. B., & Dvorkin, C. 2021, *PhRvD*, **103**, 023504
- Dvorkin, C., Gerbino, M., Alonso, D., et al. 2019, *BAAS*, **51**, 64
- Endo, A., Karatsu, K., Laguna, A. P., et al. 2019, *JATIS*, **5**, 035004
- Esteban, I., Gonzalez-Garcia, M. C., Hernandez-Cabezudo, A., Maltoni, M., & Schwetz, T. 2019, *JHEP*, **01**, 106
- Follin, B., Knox, L., Millea, M., & Pan, Z. 2015, *PhRvL*, **115**, 091301
- Fonseca, J., Silva, M., Santos, M. G., & Cooray, A. 2017, *MNRAS*, **464**, 1948
- Garmy, M., Konstandin, T., Sagunski, L., & Viel, M. 2021, *JCAP*, **03**, 049
- Garmy, M., & Taule, P. 2021, *JCAP*, **01**, 020
- Goldsmith, P. F., Langer, W. D., Pineda, J. L., & Velusamy, T. 2012, *ApJS*, **203**, 13
- Gong, Y., Chen, X., & Cooray, A. 2020, *ApJ*, **894**, 152
- Gong, Y., Cooray, A., Silva, M. B., Santos, M. G., & Lubin, P. 2011, *ApJL*, **728**, L46
- Green, D., Yang, Y.-L., Megeath, T., et al. 2019, *BAAS*, **51**, 159
- Grohs, E., Fuller, G. M., Kishimoto, C. T., Paris, M. W., & Vlasenko, A. 2016, *PhRvD*, **93**, 083522
- Hahn, C., & Villaescusa-Navarro, F. 2021, *JCAP*, **04**, 029
- Hahn, C., Villaescusa-Navarro, F., Castorina, E., & Scoccimarro, R. 2020, *JCAP*, **03**, 040
- Hall, A. C., & Challinor, A. 2012, *MNRAS*, **425**, 1170
- Hannestad, S. 2005, *PhRvL*, **95**, 221301
- Hannestad, S., Upadhye, A., & Wong, Y. Y. 2020, *JCAP*, **11**, 062
- Herrera-Camus, R., Bolatto, A. D., Wolfire, M. G., et al. 2015, *ApJ*, **800**, 1
- Herter, T., Battaglia, N., Basu, K., et al. 2019, *BAAS*, **51**, 213
- Hu, W., & Eisenstein, D. J. 1998, *ApJ*, **498**, 497
- Hu, W., Eisenstein, D. J., & Tegmark, M. 1998, *PhRvL*, **80**, 5255
- Hu, W., & Sugiyama, N. 1996, *ApJ*, **471**, 542
- Hui, L., & Parfrey, K. P. 2008, *PhRvD*, **77**, 043527
- Kamenetzky, J., Rangwala, N., Glenn, J., Maloney, P. R., & Conley, A. 2016, *ApJ*, **829**, 93
- Karkare, K. S., Barry, P. S., Bradford, C. M., et al. 2020, *JLTP*, **199**, 849
- Karkare, K. S., & Bird, S. 2018, *PhRvD*, **98**, 043529
- Keating, G. K., Marrone, D. P., Bower, G. C., et al. 2016, *ApJ*, **830**, 34
- Keating, G. K., Marrone, D. P., Bower, G. C., & Keenan, R. P. 2020, *ApJ*, **901**, 141
- Keating, G. K., Bower, G. C., Marrone, D. P., et al. 2015, *ApJ*, **814**, 140
- Kennicutt, R. C., Jr. 1998, *ARA&A*, **36**, 189
- Kogut, A., Dwek, E., & Moseley, S. H. 2015, *ApJ*, **806**, 234
- Kovetz, E. D., Viero, M. P., Lidz, A., et al. 2017, arXiv:1709.09066
- Lagache, G., Cousin, M., & Chatzikos, M. 2018, *A&A*, **609**, A130
- Lattanzi, M., & Gerbino, M. 2018, *FrP*, **5**, 70
- Lesgourgues, J., Mangano, G., Miele, G., & Pastor, S. 2013, *Neutrino Cosmology* (Cambridge: Cambridge Univ. Press)
- Lesgourgues, J., Pastor, S., & Perotto, L. 2004, *PhRvD*, **70**, 045016
- Li, T. Y., Wechsler, R. H., Devaraj, K., & Church, S. E. 2016, *ApJ*, **817**, 169
- Lidz, A., Furlanetto, S. R., Oh, S. P., et al. 2011, *ApJ*, **741**, 70
- Lidz, A., & Taylor, J. 2016, *ApJ*, **825**, 143
- Linder, E. V. 2003, *PhRvL*, **90**, 091301
- Liu, A., Pritchard, J. R., Allison, R., et al. 2016, *PhRvD*, **93**, 043013
- Liu, R. H., & Breyse, P. C. 2021, *PhRvD*, **103**, 063520
- Lorenz, C. S., Calabrese, E., & Alonso, D. 2017, *PhRvD*, **96**, 043510
- LoVerde, M. 2014, *PhRvD*, **90**, 083530
- Mangano, G., Miele, G., Pastor, S., et al. 2005, *NuPhB*, **729**, 221
- Massara, E., Villaescusa-Navarro, F., Ho, S., Dalal, N., & Spergel, D. N. 2021, *PhRvL*, **126**, 011301
- Masui, K. W., Switzer, E. R., Banavar, N., et al. 2013, *ApJL*, **763**, L20
- Mishra-Sharma, S., Alonso, D., & Dunkley, J. 2018, *PhRvD*, **97**, 123544
- Moradinezhad Dizgah, A., & Keating, G. K. 2019, *ApJ*, **872**, 126
- Moradinezhad Dizgah, A., Keating, G. K., & Fialkov, A. 2019, *ApJL*, **870**, L4
- Moradinezhad Dizgah, A., Nikakhtar, F., Keating, G. K., & Castorina, E. 2021, arXiv:2111.03717
- Moriwaki, K., Filippova, N., Shirasaki, M., & Yoshida, N. 2020, *MNRAS*, **496**, L54

- Muñoz, J. B., & Dvorkin, C. 2018, *PhRvD*, **98**, 043503
- Naess, S., Aiola, S., Austermann, J. E., et al. 2020, *JCAP*, **12**, 046
- Nasirudin, A., Murray, S. G., Trott, C. M., et al. 2020, *ApJ*, **893**, 118
- Obuljen, A., Castorina, E., Villaescusa-Navarro, F., & Viel, M. 2018, *JCAP*, **05**, 004
- Padmanabhan, H. 2018, *MNRAS*, **475**, 1477
- Padmanabhan, H. 2019, *MNRAS*, **488**, 3014
- Paine, S. 2019, The am atmospheric model, v.11.0, Zenodo, doi:[10.5281/zenodo.3406496](https://doi.org/10.5281/zenodo.3406496)
- Pan, Z., & Knox, L. 2015, *MNRAS*, **454**, 3200
- Parfrey, K., Hui, L., & Sheth, R. K. 2011, *PhRvD*, **83**, 063511
- Patterson, R. B. 2015, *ARNPS*, **65**, 177
- Popping, G., Narayanan, D., Somerville, R. S., Faisst, A. L., & Krumholz, M. R. 2019, *MNRAS*, **482**, 4906
- Popping, G., van Kampen, E., Decarli, R., et al. 2016, *MNRAS*, **461**, 93
- Pullen, A. R., Serra, P., Chang, T.-C., Dore, O., & Ho, S. 2018, *MNRAS*, **478**, 1911
- Redford, J., Wheeler, J., Karkare, K., et al. 2018, *Proc. SPIE*, **10708**, 107081O
- Righi, M., Hernandez-Montegudo, C., & Sunyaev, R. 2008, *A&A*, **489**, 489
- Roy Choudhury, S., & Hannestad, S. 2020, *JCAP*, **07**, 037
- Roy Choudhury, S., & Naskar, A. 2019, *EPJC*, **79**, 262
- Sailer, N., Castorina, E., Ferraro, S., & White, M. 2021, *JCAP*, **2021**, 049
- Sargsyan, L., Leboutteiller, V., Weedman, D., et al. 2012, *ApJ*, **755**, 171
- Schmittfull, M., & Seljak, U. 2018, *PhRvD*, **97**, 123540
- Shirokoff, E., Barry, P. S., Bradford, C. M., et al. 2012, *Proc. SPIE*, **8452**, 84520R
- Silva, M. B., Kovetz, E. D., Keating, G. K., et al. 2021, *ExA*, **51**, 1593
- Silva, M. B., Santos, M. G., Cooray, A., & Gong, Y. 2015, *ApJ*, **806**, 209
- Speagle, J. S., Steinhardt, C. L., Capak, P. L., & Silverman, J. D. 2014, *ApJS*, **214**, 15
- Sprenger, T., Archidiacono, M., Brinckmann, T., Clesse, S., & Lesgourgues, J. 2019, *JCAP*, **02**, 047
- Sugai, H., Ade, P. A. R., Akiba, Y., et al. 2020, *JLTP*, **199**, 1107
- Sun, G., Moncelsi, L., Viero, M. P., et al. 2018, *ApJ*, **856**, 107
- Tacconi, L. J., Neri, R., Genzel, R., et al. 2013a, *ApJ*, **768**, 74
- Tacconi, L. J., Neri, R., Genzel, R., et al. 2013b, *ApJ*, **768**, 74
- Upadhye, A. 2019, *JCAP*, **05**, 041
- Vagnozzi, S., Dhawan, S., Gerbino, M., et al. 2018, *PhRvD*, **98**, 083501
- Valcin, D., Villaescusa-Navarro, F., Verde, L., & Raccanelli, A. 2019, *JCAP*, **12**, 057
- Vallini, L., Pallottini, A., Ferrara, A., et al. 2018, *MNRAS*, **473**, 271
- Viljoen, J.-A., Fonseca, J., & Maartens, R. 2021, *JCAP*, **2021**, 010
- Villaescusa-Navarro, F., Marulli, F., Viel, M., et al. 2014, *JCAP*, **03**, 011
- Visbal, E., & Loeb, A. 2010, *JCAP*, **1011**, 016
- Yang, S., Popping, G., Somerville, R. S., et al. 2021, arXiv:2108.07716
- Yu, B., Knight, R. Z., Sherwin, B. D., et al. 2018, arXiv:1809.02120